Figure 4
Cardiac-MLCK regulates the initiation of sarcomere assembly in cultured cardiomyocytes through MLC2v phosphorylation. Original magnification, ×1,000 (upper and lower panels); ×2,000 (middle panels). (**A–F**) Cardiomyocytes were transfected with control siRNA (**A–C**) or si-cMK (**D–F**). Middle panels show higher magnification of boxed regions in top panels. In serum-containing conditions, si-cMK–transfected cardiomyocytes showed reduced levels of MLC2v phosphorylation (**D**) compared with control siRNA–transfected cardiomyocytes (**A**), although both exhibited regularly organized sarcomere structures. Actin staining in cardiomyocytes cultured in serum-free conditions revealed a punctuated pattern in the sarcomeres (**B** and **E**); moreover, the degree of MLC2v phosphorylation was reduced in the si-cMK–transfected cardiomyocytes compared with the control siRNA–transfected cardiomyocytes. Stimulation with 2 μM epinephrine provoked upregulation of MLC2v phosphorylation and sarcomere reassembly in control siRNA–transfected cardiomyocytes (**C**), but not in si-cMK–transfected cardiomyocytes (**F**). (**G**) We confirmed the levels of MLC2v phosphorylation shown in **A–F** using immunoblot analysis. (**H**) Quantitation of the levels of phosphorylated MLC2v shown in **G**. Values are mean ± SEM. (**I**) Percentage of the cells with organized sarcomeres. There was no significant difference between the populations of cardiomyocytes transfected with control siRNA and si-cMK under either serum-containing or serum-free conditions. The percentage of the cells with organized sarcomeres was significantly higher for the control siRNA–transfected cardiomyocytes than for the si-cMK–transfected cardiomyocytes. Values are mean ± SEM. p-MLC2v, phosphorylated MLC2v. $**P < 0.001$.

MOs effectively deleted the targeted exons, inducing comparable ventral swelling phenotypes (Figure 6, D–F). The finding that 4 different MOs produced similar results suggests that the cardiac phenotypes resulted from a loss of the kinase activity of z–cardiac-MLCK. To evaluate the cardiac phenotype of the z-cMKaugMO morphants in detail, we examined the SAG4A zebrafish strain, which specifically expresses GFP in the cardiac ventricle (14). After injecting z-cMKaugMO into SAG4A embryos, cardiac motion at 72 hpf was imaged with a high-sensitivity digital camera attached to a fluorescence stereomicroscope (Figure 6G and Supplemental

Movies 1 and 2; supplemental material available online with this article; doi:10.1172/JCI30804DS1). Recordings were converted to motion mode (M-mode) images using our original software (Figure 6H). From these images, we determined the end-diastolic dimension (Dd), end-systolic dimension (Ds), and fractional shortening (FS) of the cardiac ventricle. These data are summarized in Table 2, and the results indicate that the cardiac dimensions of the z-cMKaugMO morphants were significantly larger than those of control zebrafish embryos (Dd, 79.6 ± 3.7 versus 117.0 ± 10.4 μm; Ds, 50.3 ± 6.5 versus 76.0 ± 7.0 μm; $P < 0.0001$ for both com-
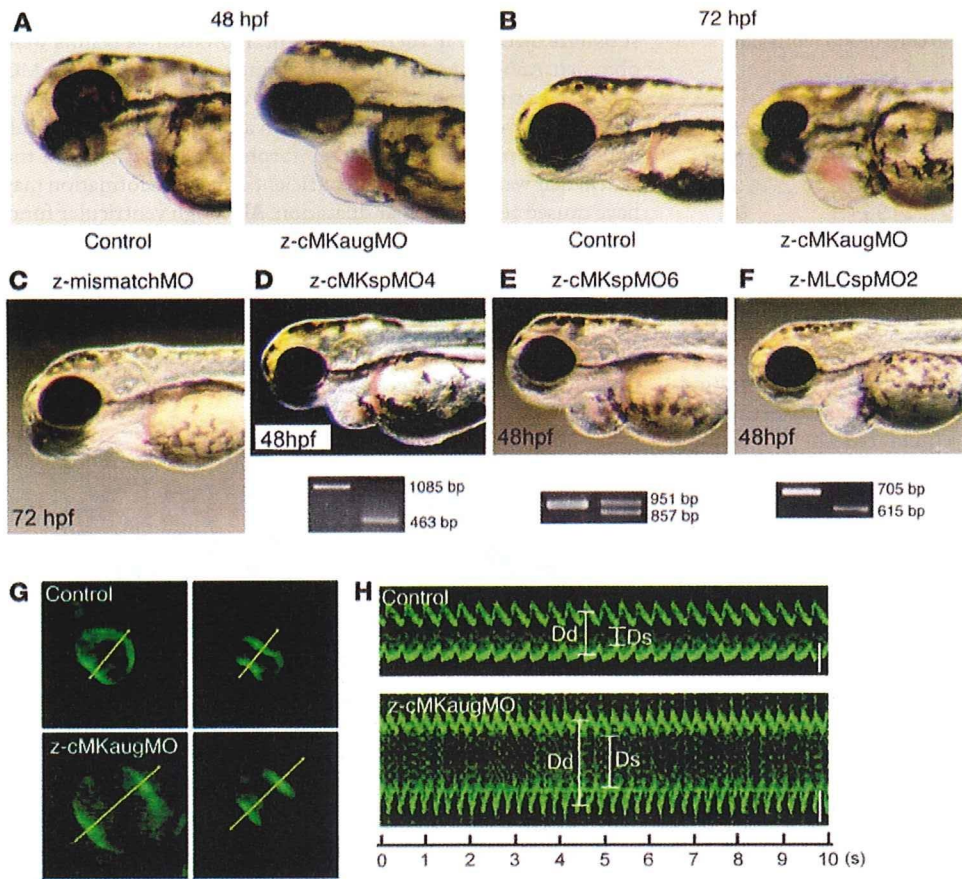
A

Figure 5
Cardiac-MLCK is highly conserved in several vertebrates, including zebrafish. (**A**) Cardiac-MLCK is evolutionarily conserved in vertebrates, including humans (Hu), dogs (Ca), mice (Mm), chickens (Gg), and zebrafish (z), with the highest degree of homology in the C-terminal portion of the serine/threonine kinase domain. Black backgrounds indicate identical amino acids. Amino acids in the ATP-binding region are shown in blue; those in the kinase active site are shown in red. (**B–I**) Whole-mount in situ hybridizations depict the expression of z–cardiac-MLCK (z-cMK) in zebrafish embryos hybridized with z–cardiac-MLCK–specific antisense probe (**B, C, F,** and **G**) or z–cardiac-MLCK sense probe (**D, E, H,** and **I**). At 24 hpf, z–cardiac-MLCK was expressed in heart precursor cells (arrow). At 48 hpf, z–cardiac-MLCK was selectively expressed in the heart (asterisks denote atrium [a] and ventricle [v]).

parisons). We did not, however, observe a significant difference in cardiac contractility as assessed by the FS (36.9% ± 7.1% versus 34.9% ± 4.1%; NS), likely because of a compensatory upregulation of inotropy. In support of this hypothesis, we observed that the heart rate was significantly higher in the z-cMKaugMO morphants (184 ± 14.5 versus 216 ± 24.7 bpm; P = 0.0017). At 5–6 days after fertilization, the z-cMKaugMO morphants developed systemic edema and died of circulatory disturbances. Histopathologic analysis demonstrated that the ventral swelling in the z-cMKaugMO morphants reflected pericardial edema. Although the cardiac atria were almost normal, the ventricular walls of the morphants were thinner than those of control zebrafish embryos (Figure 7, A–D). Transmission electron microscopy revealed that only a few poorly differentiated sarcomere structures were present in the ventricles of the z-cMKaugMO morphants (Figure 7, G–J); no other apparent abnormalities were detected in the atrial sarcomeres (Figure

7, E and F). These data suggest that cardiac-MLCK is required for sarcomere formation in the developing heart.

Cardiac-MLCK is upregulated during myofibrillogenesis and in mammalian models of heart failure. Sarcomere organization in cardiomyocytes in vivo is supposed to occur during myofibrillogenesis. In the rat heart, the mRNA and protein levels of cardiac-MLCK were upregulated from 1 week after birth through adulthood (Figure 8, A and B). The expression of cardiac-MLCK mRNA was also analyzed in mammalian models of heart failure. Myocardial infarctions (MIs) were produced in Wistar rats by permanently ligating the left anterior descending artery. At 4 weeks after the onset of MI, heart failure developed. The hemodynamic and echocardiographic parameters of the MI and sham-operated rats are summarized in Table 3. In MI rats, the LV end-diastolic pressure and LVDd were significantly higher than in sham-operated rats (LV end-diastolic pressure, 20.5 ± 8.2 versus 3.2 ± 1.0 mmHg; P < 0.01;

Figure 6
Suppression of z–cardiac-MLCK expression induced dilatation of the cardiac ventricle in zebrafish embryos. (A and B) Control mock-injected zebrafish embryos and zebrafish embryos injected with z-cMKaugMO produced the phenotype of ventral swelling at 48 hpf (A) and 72 hpf (B). (C) Zebrafish embryos injected with MOs with 5-base mismatch to z-cMKaugMO (z-mismatchMO) showed phenotypes comparable to those of controls. (D and E) Injection of specific MOs designed to interfere with the splicing of z–cardiac-MLCK exon 4 (z-cMKspMO4; D) or exon 6 (z-cMKspMO6; E) or with the splicing of z-MLC2v exon 2 (z-MLCspMO2; F), which coded for the phosphorylatable serine residue, also induced the phenotype of ventral swelling. RT-PCR products amplified from cDNA produced from the morphants were shorter than those obtained from control embryos due to the removal of the targeted exons. (G) Cardiac motion in the control embryos and z-cMKaugMO morphants. Shown are end-diastolic (left) and end-systolic (right) phases of the cardiac ventricular cycle in a control embryo and z-cMKaugMO morphant. (H) Representative M-mode images of both control embryo and z-cMKaugMO morphant hearts. Scale bars: 50 μm. Original magnification, ×20 (A–F); ×100 (G).

the results obtained with the microarray analysis of human failing myocardia.

Discussion

In this study, we performed microarray analysis of human failing myocardia to identify new genes involved in the pathophysiology of CHF. By comparing mRNA expression analysis with the clinical parameters of the patients, we identified what we believe to be a novel candidate gene, *MYLK3* (encoding cardiac-MLCK), that had not been isolated in previous microarray studies of heart failure (15). Upregulation of *MYLK3* transcription in failing myocardia was confirmed in mammalian models of heart failure, such as MI rats. In this experiment, mRNA expression of cardiac-MLCK was significantly upregulated in MI rats with heart failure, and the relative expression profile was well correlated with that of ANP, a representative marker of CHF.

MLCK family members in muscle are sarcomeric protein kinases that phosphorylate a serine residue near the amino terminus of the myosin regulatory light chain. In cardiac muscle, phosphorylation of MLC2v led to sarcomere organization, an event that represents cardiac hypertrophy in cultured neonatal rat cardiomyocytes (13). skMLCK is thought to be the predominant kinase that acts on MLC2v, and a gradient of MLC2v phosphorylation in the cardiac wall from endocardium

LVDd, 9.8 ± 0.3 versus 6.8 ± 0.5 mm; $P < 0.01$), whereas the maximum LV peak rate of change in pressure during isovolumic contraction (Max dP/dt) and FS were significantly lower than in sham-operated rats (Max dP/dt, 5,845 ± 1,156 versus 9,440 ± 644 mmHg/s; $P < 0.01$; FS, 12.0 ± 3.1 versus 44.0 ± 7.8%; $P < 0.01$). In MI rats, *MYLK3* expression was significantly upregulated compared with that in the sham-operated rats (relative cardiac-MLCK mRNA expression, 1.46 ± 0.42 versus 1.00 ± 0.15; $P < 0.05$; Figure 8C). Furthermore, the relative mRNA expression level of cardiac-MLCK was significantly correlated with that of ANP ($r = 0.778$, $P < 0.005$; Figure 8D). Upregulation of cardiac-MLCK expression in the infantile heart suggests cardiac-MLCK participates in myofibrillogenesis. Additionally, upregulation of cardiac-MLCK mRNA levels in mammalian models of heart failure confirmed

to epicardium is responsible for the generation of cardiac torsion (9). A recent study using skMLCK-deficient mice, however, revealed that removing skMLCK did not result in a cardiac phenotype (10). Furthermore, in the current study and previous studies, skMLCK expression was not detected in the heart by either Western blotting or RT-PCR (16), suggesting the existence of an as-yet unknown kinase that phosphorylates MLC2v in cardiac muscle.

We identified cardiac-MLCK, which serves as a specific kinase for MLC2v in cardiac muscle. In cultured cardiomyocytes, cardiac-MLCK regulates sarcomere assembly through the phosphorylation of MLC2v. When isolated cardiomyocytes were cultured under serum-free conditions, established sarcomere structures were disrupted. Overexpression of recombinant cardiac-MLCK and exogenous stimulation by epinephrine promoted sarcomere

Table 2

Cardiac physiological characteristics of control and morphant zebrafish embryos

	Control	Morphant	P
Dd (μm)	79.6 ± 3.7	117 ± 10.4	<0.0001
Ds (μm)	50.3 ± 6.5	76.0 ± 7.0	<0.0001
FS (%)	36.9 ± 7.1	34.9 ± 4.1	NS
HR (bpm)	184 ± 14.5	216 ± 24.7	0.0017

Values are mean ± SEM. n = 12 per group. HR, heart rate.

reassembly through MLC2v phosphorylation. Similar findings have previously been reported using recombinant constitutively active skMLCK (13). We further elucidated the physiologic roles of endogenous cardiac-MLCK using siRNAs. Decreases in MLC2v phosphorylation following the introduction of si-cMK significantly impaired epinephrine-induced sarcomere reassembly. Additionally, specific knockdown of cardiac-MLCK did not affect to the expression of other sarcomere-related proteins such as troponin T, desmin, and α-actinin. These proteins are thought to have important roles in sarcomere and myofibril formation (17–19). Thus, in cardiomyocytes, phosphorylation of MLC2v by cardiac-MLCK is an essential step for the initiation of sarcomere assembly. Upregulation of the protein levels of cardiac-MLCK in infantile rat heart supports this idea.

In this experimental model, no phenotypic alterations were observed following knockdown of cardiac-MLCK in cultured cardiomyocytes. This apparently paradoxical result occurred because phosphorylation of MLC2v is upregulated in cultured cardiomyocytes until 36 hours after plating, after which it is gradually downregulated. In the siRNA-mediated gene knockdown experiment, a reduction in the cardiac-MLCK protein level that was sufficient to decrease the phosphorylation of MLC2v was only obtained 60–72 hours after isolation. Therefore, by the time the required level of protein suppression was achieved, primary sarcomere assembly had been completed, and the subsequent decreases in MLC2v phosphorylation did not disrupt established sarcomere structures.

Reduction of cardiac-MLCK levels in zebrafish embryos through the injection of z-cMKaugMO resulted in ventral swelling, which has been previously reported to be a representative phenotype of cardiac abnormalities in zebrafish embryos (20, 21). The reliability of the results obtained with z-cMKaugMO was confirmed using

multiple MOs that targeted not only cardiac-MLCK but also its substrate, MLC2v. In each experiment, reproducible results were obtained. Another MO that has 5-base mismatch to z-cMKaugMO was also examined as a negative control MO. Further analysis revealed dilatation of the ventricle with a thinned ventricular wall and immature sarcomeres in the morphants. The fragility of the ventricular wall as a result of insufficient sarcomere formation may have caused the ventricular dilatation. Although ventricular function as assessed by FS was preserved in the morphants, this might have been due to some positive inotropic effects, which were suggested by the increased heart rate observed in the z-cMKaugMO morphants. Although several reports have investigated the effects of MLC2v phosphorylation in striated muscle contractions, including in cardiac muscle, the in vivo ventricular role of MLC2v phosphory-

Figure 7
Histology of the zebrafish heart at 48 hpf. (**A–D**) Longitudinal sections stained with hematoxylin and eosin. Scale bars: 50 μm. (**E–J**) Transmission electron micrographs. Scale bars: 2 μm. (**A** and **B**) Histology of control zebrafish hearts at 48 hpf. A relatively thick ventricular wall was apparent (**B**, arrowheads). (**C** and **D**) Pericardial edema and a thinner ventricular wall (**D**, arrowheads) were observed in z-cMKaugMO morphants. (**E** and **F**) In the atria, the sarcomere structures were well differentiated in both the control embryos and the z-cMKaugMO morphants. In the ventricles of control embryos, robust sarcomere structures were observed (**G** and **H**), whereas the ventricles of the z-cMKaugMO morphants contained sparse and immature sarcomere structures (**I** and **J**). Images in **B**, **D**, **H**, and **J** show higher magnifications of the boxed areas in **A**, **C**, **G**, and **I**, respectively. Asterisks denote sarcomere structures (s).
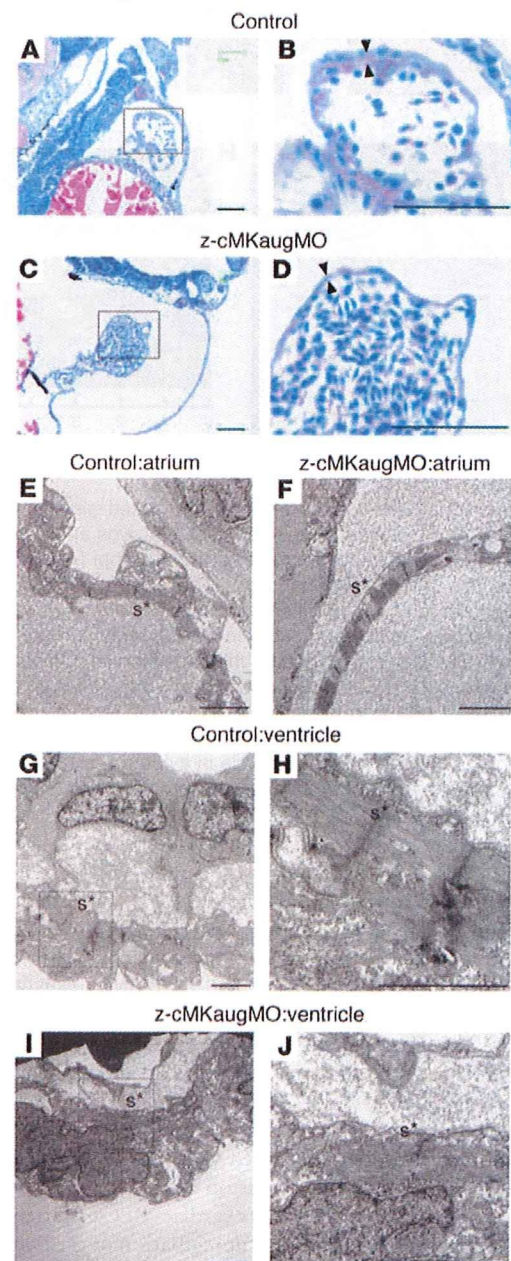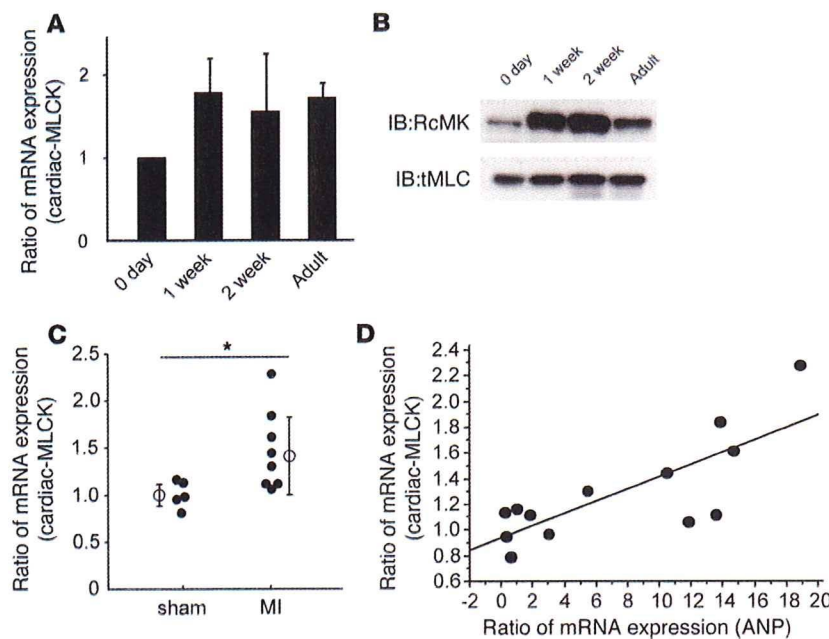
Figure 8
Expression of cardiac-MLCK is upregulated in infantile rat myocardia and failing rat myocardia. (**A**) mRNA expression of cardiac-MLCK was also upregulated in rat myocardia from 1 week after birth to adulthood. The levels of cardiac-MLCK protein were upregulated in infantile myocardia 1–2 weeks after birth. (**B**) The levels of cardiac-MLCK protein were upregulated in infantile myocardia 1–2 weeks after birth. (**C**) mRNA expression of cardiac-MLCK was significantly upregulated in failing rat myocardia. $n = 5$ (sham-operated); 8 (MI). Filled symbols represent values from individual mice; open symbols with bars represent mean ± SEM. *$P < 0.05$. (**D**) The relative mRNA expression levels of ANP and cardiac-MLCK were significantly correlated ($r = 0.778$; $P < 0.005$).

lation is still not well understood (22, 23). To explore how cardiac-MLCK contributes to ventricular function, other experiments, such as a skinned fiber study, should be performed. A similar cardiac phenotype was reported in a recent study investigating the zebrafish *tel* mutant, in which the gene encoding MLC2v was disrupted by an *N*-ethyl-*N*-nitrosourea-induced mutation. The authors concluded that MLC2v is essential for the assembly of myosin thick filament (24). The observation of incomplete sarcomere formation resulting in a dilated ventricle in zebrafish embryos after injection of z-cMKaugMO can be explained by an inability to initiate sarcomere assembly as a result of reduced cardiac-MLCK levels.

Our results prompt the important question of how cardiac-MLCK is involved in the pathophysiology of CHF. In failing myocardia, decreases in myofibrillar proteins such as titin, myosin, and actin, together with the sarcomere defects, have been identified (25, 26). Reduced expression of MLC2v protein as a result of protease-mediated cleavage and reduced phosphorylation of MLC2v have also been reported in the myocardia of patients with dilated cardiomyopathy. These changes produced unstable, short myofilaments following defective assembly of the myosin thick filaments (27, 28). Our preliminary data also revealed that the protein expression of cardiac-MLCK and the extent of MLC2v phosphorylation were remarkably decreased in failing myocardia of trans-aortic constriction mice compared with those of sham-operated mice. Previous reports and our present results suggest that cardiac-MLCK may be upregulated to compensate for the lower expression and reduced phosphorylation of MLC2v. As a possible therapeutic modality in patients with CHF, upregulation of cardiac-MLCK may promote sarcomere reassembly and enhanced contractility of the failing heart.

Methods

Animals. All procedures were performed in conformity with the *Guide for the care and use of laboratory animals* (NIH publication no. 85-23, revised 1996) and were approved by the Osaka University Committee for Laboratory Animal Use.

Materials. We used commercially available anti-FLAG-M2 antibody and anti-FLAG-M2 affinity gel (Sigma-Aldrich), monoclonal mouse anti-troponin T cardiac isoform antibody (NeoMarkers), monoclonal mouse anti-human desmin Antibody (Dako Corp.), and polyclonal goat anti–α-actinin (N-19) antibody (Santa Cruz Biotechnology Inc.). Epinephrine hydrochloride was purchased from Sigma-Aldrich. We also generate RcMK, anti-human smMLCK, tMLC, and p-s15MLC.

Microarray analysis. For microarray analysis, 2 RNA samples of human normal myocardium and 12 samples of failing myocardium were used. Failing myocardium samples were obtained from severe CHF patients by Batista or Dor operation after obtaining the patients' written informed consent. PAP was measured 2–4 weeks before the operation, and ejection fraction (EF) was measured by echocardiography the day before the operation. Normal samples were purchased from Biochain Inc. Cardiac gene expression was determined using the HG-U95 Affymetrix GeneChip. All expression data were normalized by global scaling and analyzed by GeneSpring software (Agilent Technologies). All expression data were normalized per gene and analyzed after removing noise and unreliable data. PAP, EF, and BNP values were normalized to their median values, and the correlation between gene expression and the clinical parameters was evalu-

Table 3
Hemodynamic and echocardiographic characteristics of MI and sham-operated rats

	Sham	MI	P
LVSP (mmHg)	126.8 ± 10.9	125.5 ± 11.0	NS
HR (bpm)	415.4 ± 10.4	407.6 ± 23.0	NS
Max dP/dt (mmHg/s)	9,440 ± 644	5,845 ± 1,156	<0.01
LVEDP (mmHg)	3.2 ± 1.0	20.5 ± 8.2	<0.01
LVDd (mm)	6.8 ± 0.5	9.8 ± 0.3	<0.01
FS (%)	44.0 ± 7.8	12.0 ± 3.1	<0.01

Values are mean ± SEM. $n = 5$ (sham); 8 (MI). LVEDP, LV end-diastolic pressure; LVSP, LV systolic pressure; HR, heart rate; Max dP/dt, LV peak rate of change in pressure during isovolumic contraction.

ated. To further select genes that are expressed almost exclusively in heart, expression values for the candidate genes were retrieved in 24 major tissues for analysis from GeneExpress database (Gene Logic Inc.) containing GeneChip expression profiles of human samples.

RNA extraction, RT-PCR, and quantification. Rat tissues (20–50 mg) and zebrafish embryos at 72 hpf were homogenized in 1 ml RNA-Bee reagent (Tel-Test Inc.), and total RNA was isolated and converted to cDNA using Omniscript RT kit (QIAGEN) according to the manufacturer's instructions. Specific primers to amplify rat ANP, β myosin heavy chain, cardiac-MLCK, and GAPDH mRNA were purchased from Applied Biosystems. Quantitative RT-PCR reactions were run in duplicate using the ABI Prism 7700 Sequence Detector System (Applied Biosystems). The level of each transcript was quantified by the threshold cycle (Ct) method using GAPDH as an endogenous control. For RT-PCR, specific primers that cover the region of targeted exons were designed to amplify the transcripts of z–cardiac-MLCK and z-MLC2v. See Supplemental Methods for primer sequences.

Northern blot analysis. Commercially available human multiple tissue Northern blot and polyA⁺ RNA of human heart and skeletal muscle were purchased from Clontech. Each polyA⁺ RNA was reverse transcribed and amplified using an Omniscript RT kit (QIAGEN) according to the manufacturer's protocol. Hybridization probes of human cardiac-MLCK and smMLCK were amplified by PCR from cDNA of human heart, and a hybridization probe of human skMLCK was amplified by PCR from cDNA of human skeletal muscle. Membrane was hybridized to ^{32}P-labeled probe in Rapid-Hyb buffer (Amersham Bioscience) at 65°C for 1 hour. Final wash conditions were 0.1× SSC with 0.1% SDS at 65°C for 5 minutes. Hybridized membrane was visualized by autoradiography using the BAS system (Fuji).

Preparation and transfection of adenovirus constructs. Adenovirus constructs were generated using ViraPower Adenoviral Expression System (Invitrogen) essentially as instructed by the manufacturer. Adenovirus vectors encoding murine cardiac-MLCK and LacZ were infected to cultured cardiomyocytes for 12 hours in various MOIs. Protein collection and immunostaining were performed 48 hours after adenovirus infection.

Identification of the substrate of cardiac-MLCK. Recombinant cardiac-MLCK was expressed in HEK293T cells as FLAG-tagged protein. HEK293T cells expressing FLAG-tagged cardiac-MLCK were lysed with cell lysis buffer (20 mM MOPS, pH 7.0, 0.15 M NaCl, 10% glycerol, and 1% CHAPS) and recombinant cardiac-MLCK was purified by immunoprecipitation using anti-FLAG-M2 affinity gel (Sigma-Aldrich). Hearts dissected from male C57BL/6 mice (10–12 weeks of age) were mechanically homogenized using a Polytron homogenizer in 10 ml of tissue lysis buffer (30 mM MOPS, pH 6.8, 5% glycerol, 0.1% 2-mercaptoethanol, and 1 mM EGTA). Lysate was centrifuged for 40 minutes at 100,000 g, and 9 ml of supernatant was collected. Murine heart extracts were then applied to SP650 cation exchange column. The column was equilibrated with elution buffer A (30 mM MOPS, 5% glycerol, 0.1% 2-mercaptoethanol) at pH 6.8, and the extracts were eluted with a linear gradient of NaCl (0–0.5 M) at a flow rate of 1 ml/min. Each 1-ml fraction collected was incubated for 30 minutes with activated recombinant cardiac-MLCK, commercially available recombinant calmodulin (Upstate), 2 mM CaCl₂, and [γ-P³²]ATP and then subjected to SDS-PAGE. After drying, the gel was autoradiographed and visualized with BAS (Fuji). The fractions containing 20-kDa substrate (fractions 10 and 11) labeled with [γ-P³²]ATP were pooled and applied to a phenyl-RPLC column (5Ph-AR-300; nacalai tesque) equilibrated with 0.3% trifluoroacetic acid and 5% acetoritrile. Fractions were eluted with a linear gradient of 100% acetonitrile at flow rate of 1 ml/min. After separation with SDS-PAGE, the gel was simultaneously silver stained and autoradiographed. After identifying the 20-kDa substrate with silver-stained gel, the bands were excised from the gel, and proteins were identified by matrix-

assisted laser desorption/ionization-time-of-flight mass spectrometry and peptide mass fingerprinting.

Preparation of cultured neonatal rat cardiomyocytes and gene silencing via RNA interference. Primary cultures of neonatal cardiomyocytes were prepared from Wistar rats as described previously (29). Cardiomyocytes were cultured in DMEM (Sigma-Aldrich) supplemented with 10% FBS (Equitech-Bio). At 6 hours after isolation of cardiomyocytes, cells were transfected with siRNAs (100 nmol/l) using Optifect reagent (Invitrogen) according to the manufacturer's instructions. Both si-cMK (see Supplemental Methods) and si-smMK (see Supplemental Methods) were purchased from B-bridge. As a negative control, cells were transfected with siControl Non-Targeting siRNA#1 (B-bridge). Isolation of mRNA was performed at 24 hours after transfection and protein experiments were performed at 72 hours after transfection. For immunostaining, the same procedures of siRNA transfection were performed in one-fifth scale on Lab-Tek Chamber Slides (nunc).

Cloning of z–cardiac-MLCK. We generated an adult zebrafish cDNA library in Lambda Zap II (Stratagene) using polyA⁺ RNA from adult zebrafish. The cDNA library was screened with the probe designed to the 5′ side in the ORF of the putative zebrafish ortholog of cardiac-MLCK sequence. Positive phage clone was determined by using phage plaque screen method and single clone excision protocol according to the manufacturer's instructions (Stratagene).

Gene accession numbers. DDBJ accession numbers for the zebrafish MLCK family were as follows: cardiac-MLCK, AB267907; smMLCK, AB267908; skMLCK, AB267909.

Whole-mount in situ hybridization. The digoxigenin-labeled antisense and sense RNA probes (see Supplemental Methods) were transcribed using SP6 and T7 RNA polymerase. Zebrafish embryos at 24 and 48 hpf were fixed with 4% paraformaldehyde, digested with proteinase K, and hybridized with each probe at 68°C. Alkaline-conjugated anti-digoxigenin antibody was used to detect the signals. After staining, embryos were refixed with 4% paraformaldehyde and stored in PBS.

Injection of MO. All MOs were synthesized by Gene-Tools. At cell stages 1–4, 4–10 ng of these MOs were injected into zebrafish embryos. Several data were collected before the 96-hpf stage. Sequences of MOs are available in the Supplemental Methods.

Analysis of zebrafish cardiac histology and cardiac function. We studied hearts of control mock-injected zebrafish embryos and z-cMKaugMO–injected zebrafish embryos at 72 hpf by routine histopathology including transmission electron micrography. To visualize the motion of zebrafish cardiac ventricle, the SAG4A strain of zebrafish, which specifically expresses GFP in its cardiac ventricular wall (14), was applied to MO-mediated gene knockdown experiments. GFP-expressed control mock-injected and z-cMKaugMO–injected zebrafish hearts at 72 hpf were imaged with Leica digital camera DFC 350 FX on a Leica MZ 16 FA fluorescence stereomicroscope. Acquired images were compiled as digital movie files using Leica FW4000 software. Each recorded movie was converted to M-mode image using our original software, and Dd, Ds, FS, and heart rate were measured from the M-mode images.

Experimental protocols of rats. Male Wistar rats (0 days, 1 week, 2 weeks, and 10 weeks for mRNA and protein expression analysis; 8 weeks for production of MI rats; Japan Animals) were used in these experiments. MI was induced by permanent ligation of the left anterior descending coronary artery as previously described (29). The same surgical procedure was performed in a sham-operated group of rats except that the suture around the coronary artery was not tied. Isolation of total RNA was performed at 4 weeks after the onset of MI from noninfarcted myocardiums of resected LVs.

Statistics. Statistical analysis was performed using Mann-Whitney *U* test and single regression analysis. Data are presented as mean ± SEM. A *P* value less than 0.05 was considered significant.

Acknowledgments

Address correspondence to: Seiji Takashima, Department of Cardiovascular Medicine, Health Care Center, Osaka University Graduate School of Medicine, 2-2 Yamadaoka, Suita, Osaka 565-0871, Japan. Phone: 011-816-8679-3472; Fax: 011-816-8679-3473; E-mail: takasima@medone.med.osaka-u.ac.jp.

1. Jessup, M., and Brozena, S. 2003. Heart failure. N. Engl. J. Med. **348**:2007-2018.
2. Kamisago, M., et al. 2000. Mutations in sarcomere protein genes as a cause of dilated cardiomyopathy. N. Engl. J. Med. **343**:1688-1696.
3. Olson, T.M., Michels, V.V., Thibodeau, S.N., Tai, Y.S., and Keating, M.T. 1998. Actin mutations in dilated cardiomyopathy, a heritable form of heart failure. Science. **280**:750-752.
4. Watkins, H., et al. 1995. Mutations in the cardiac myosin binding protein-C gene on chromosome 11 cause familial hypertrophic cardiomyopathy. Nat. Genet. **11**:434-437.
5. Collins, J.H. 2006. Myoinformatics report: myosin regulatory light chain paralogs in the human genome. J. Muscle Res. Cell Motil. **27**:69-74.
6. Chen, J., et al. 1998. Selective requirement of myosin light chain 2v in embryonic heart function. J. Biol. Chem. **273**:1252-1256.
7. Olsson, M.C., Patel, J.R., Fitzsimons, D.P., Walker, J.W., and Moss, R.L. 2004. Basal myosin light chain phosphorylation is a determinant of Ca2+ sensitivity of force and activation dependence of the kinetics of myocardial force development. Am. J. Physiol. Heart Circ. Physiol. **287**:H2712-H2718.
8. Kamm, K.E., and Stull, J.T. 2001. Dedicated myosin light chain kinases with diverse cellular functions. J. Biol. Chem. **276**:4527-4530.
9. Davis, J.S., et al. 2001. The overall pattern of cardiac contraction depends on a spatial gradient of myosin regulatory light chain phosphorylation. Cell. **107**:631-641.
10. Zhi, G., et al. 2005. Myosin light chain kinase and myosin phosphorylation effect frequency-dependent potentiation of skeletal muscle contraction. Proc. Natl. Acad. Sci. U. S. A. **102**:17519-17524.
11. Lazar, V., and Garcia, J.G. 1999. A single human myosin light chain kinase gene (MLCK; MYLK). Genomics. **57**:256-267.
12. Ruppel, K.M., Uyeda, T.Q., and Spudich, J.A. 1994. Role of highly conserved lysine 130 of myosin motor domain. In vivo and in vitro characterization of site specifically mutated myosin. J. Biol. Chem. **269**:18773-18780.
13. Aoki, H., Sadoshima, J., and Izumo, S. 2000. Myosin light chain kinase mediates sarcomere organization during cardiac hypertrophy in vitro. Nat. Med. **6**:183-188.
14. Kawakami, K., et al. 2004. A transposon-mediated gene trap approach identifies developmentally regulated genes in zebrafish. Dev. Cell. **7**:133-144.
15. Sharma, U.C., Pokharel, S., Evelo, C.T., and Maessen, J.G. 2005. A systematic review of large scale and heterogeneous gene array data in heart failure. J. Mol. Cell. Cardiol. **38**:425-432.
16. Herring, B.P., Dixon, S., and Gallagher, P.J. 2000. Smooth muscle myosin light chain kinase expression in cardiac and skeletal muscle. Am. J. Physiol. Cell Physiol. **279**:C1656-C1664.
17. Sehnert, A.J., et al. 2002. Cardiac troponin T is essential in sarcomere assembly and cardiac contractility. Nat. Genet. **31**:106-110.
18. Bar, H., et al. 2005. Severe muscle disease-causing desmin mutations interfere with in vitro filament assembly at distinct stages. Proc. Natl. Acad. Sci. U. S. A. **102**:15099-15104.
19. Ehler, E., Rothen, B.M., Hammerle, S.P., Komiyama, M., and Perriard, J.C. 1999. Myofibrillogenesis in the developing chicken heart: assembly of Z-disk, M-line and the thick filaments. J. Cell Sci. **112**:1529-1539
20. Schonberger, J., et al. 2005. Mutation in the transcriptional coactivator EYA4 causes dilated cardiomyopathy and sensorineural hearing loss. Nat. Genet. **37**:418-422.
21. Ebert, A.M., et al. 2005. Calcium extrusion is critical for cardiac morphogenesis and rhythm in embryonic zebrafish hearts. Proc. Natl. Acad. Sci. U. S. A. **102**:17705-17710.
22. Davis, J.S., Satorius, C.L., and Epstein, N.D. 2002. Kinetic effects of myosin regulatory light chain phosphorylation on skeletal muscle contraction. Biophys. J. **83**:359-370.
23. Dias, F.A., et al. 2006. The effect of myosin regulatory light chain phosphorylation on the frequency-dependent regulation of cardiac function. J. Mol. Cell. Cardiol. **41**:330-339.
24. Rottbauer, W., et al. 2006. Cardiac myosin light chain-2: a novel essential component of thick-myofilament assembly and contractility of the heart. Circ. Res. **99**:323-331.
25. Schaper, J., et al. 1991. Impairment of the myocardial ultrastructure and changes of the cytoskeleton in dilated cardiomyopathy. Circulation. **83**:504-514.
26. Hein, S., Kostin, S., Heling, A., Maeno, Y., and Schaper, J. 2000. The role of the cytoskeleton in heart failure. Cardiovasc. Res. **45**:273-278.
27. van der Velden, J., et al. 2003. The effect of myosin light chain 2 dephosphorylation on Ca2+ -sensitivity of force is enhanced in failing human hearts. Cardiovasc. Res. **57**:505-514.
28. Margossian, S.S., et al. 1992. Light chain 2 profile and activity of human ventricular myosin during dilated cardiomyopathy. Identification of a causal agent for impaired myocardial function. Circulation. **85**:1720-1733.
29. Wakeno, M., et al. 2006. Long-term stimulation of adenosine A2b receptors begun after myocardial infarction prevents cardiac remodeling in rats. Circulation. **114**:1923-1932.

ADAMTS13 assays and ADAMTS13-deficient mice

Toshiyuki Miyata, Koichi Kokame, Fumiaki Banno, Yongchol Shin and Masashi Akiyama

Purpose of review
Thrombotic thrombocytopenic purpura can be induced by acquired or congenital deficiency of the plasma von Willebrand factor-cleaving protease, ADAMTS13. Measurement of ADAMTS13 activity is important for the diagnosis and treatment of microangiopathies including thrombotic thrombocytopenic purpura. Phenotypic analysis of mice lacking the *Adamts13* gene is valuable for understanding the pathogenesis of microangiopathies.
Recent findings
The minimum substrate for ADAMTS13 activity was identified as 73 amino acid residues in the A2 domain of von Willebrand factor, called VWF73. Several new assays have been developed using this sequence. The VWF73-based assays are rapid, quantitative, and easy to handle, and are well correlated with the measures from previous assays. Mice lacking the *Adamts13* gene were produced. The mice were viable and fertile. They showed a prothrombotic state but no symptoms of spontaneous thrombocytopenia, hemolytic anemia, or microvascular thrombosis were observed.
Summary
VWF73-based ADAMTS13 assays will significantly facilitate the accurate diagnosis of microangiopathies and contribute to the improved clinical treatment of these diseases. Accumulated clinical information on patients with ADAMTS13 deficiency and mice lacking the *Adamts13* gene indicates that additional environmental or genetic susceptibility factors are required to trigger thrombotic thrombocytopenic purpura.

Keywords
ADAMTS13, microangiopathy, thrombotic thrombocytopenic purpura, von Willebrand factor

Correspondence to Toshiyuki Miyata, National Cardiovascular Center Research Institute, 5-7-1 Fujishirodai, Suita, Osaka 565-8565, Japan
Tel: +81 6 6833 5012 ext 2512, 8123; fax: +81 6 6835 1176;
e-mail: miyata@ri.ncvc.go.jp

Introduction

Thrombotic thrombocytopenic purpura (TTP) is characterized by thrombocytopenia and microangiopathic hemolytic anemia accompanied by variable-penetrance of neurologic dysfunction, renal failure, and fever. In the microvasculature of patients with TTP, systemic platelet thrombi are developed, largely resulting from the accumulation of ultralarge von Willebrand factor (ULVWF) multimers [1]. ULVWF can be accumulated by acquired or congenital deficiency of the von Willebrand factor (VWF)-cleaving protease, ADAMTS13 (a disintegrin-like and metalloprotease with thrombospondin type 1 motif, 13) [2,3**]. TTP caused by congenital deficiency of ADAMTS13 is also called Upshaw–Schulman syndrome.

Since the cloning of its cDNA in 2001, this new antithrombotic factor has been intensively studied [4–6,7*,8**, 9**,10*]. Here we summarize the recent progress on ADAMTS13, focusing on assays for ADAMTS13 and mice lacking the *Adamts13* gene.

Genetic mutations in congenital ADAMTS13 deficiency

ADAMTS13 consists of 1427 amino acid residues with a calculated molecular mass of 145 kDa. It is composed of multiple discrete domains, as shown in Fig. 1 [4–6,7*,8**, 9**]. Unlike other ADAMTS family members, the ADAMTS13 sequence has a short pro-sequence and two C-terminal CUB [complement components C1r/C1s, Uegf (epidermal growth factor-related sea urchin protein), and bone morphogenetic protein-1] domains. The human ADAMTS13 gene comprises 29 exons, encompassing 37 kb on chromosome 9q34. It is expressed mainly in the liver; primarily in stellate cells [11,12]. Platelets and endothelial cells also express ADAMTS13 [13,14,15*,16**]. The CUB domains are required for apical sorting of ADAMTS13 in endothelial cells [16**].

Figure 1 Genomic structure and domain organization of human ADAMTS13 and nonsynonymous mutations identified in patients with congenital thrombotic thrombocytopenic purpura

Missense mutations are indicated by black spades. Nonsense mutations, insertion/deletion mutations, and splice site mutations are shown by hearts, clubs, and diamonds, respectively. The P475S mutation commonly observed in the Japanese population and the A insertion at nucleotide number 4143 found in multiple European populations are shown. S, signal peptide; P, propeptide; Dis, disintegrin-like domain; T (numbered 1–8), thrombospondin type 1 motifs; CUB, complement components C1r/C1s, Uegf (epidermal growth factor-related sea urchin protein), and bone morphogenetic protein-1; Cys, cysteine-rich domain.
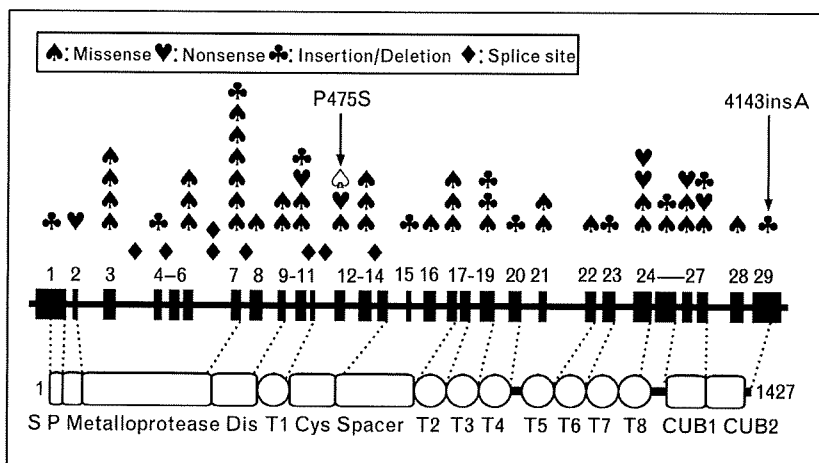
More than 60 different mutations of the *ADAMTS13* gene have been reported [6,17–19,20*,21]. More than 50% are missense mutations, as well as frame-shift mutations such as insertions and deletions, and nonsense mutations and splice-site mutations. These mutations are distributed throughout the various domains of ADAMTS13 (Fig. 1). The correlation of genotype and protease activity in some of these mutations has been examined by expression analysis *in vitro* [18,20*,21]. Most of the mutations have been identified in a single family but there are at least six recurrent mutations in unrelated patients. Among them, the 4143insA mutation has been identified as a genetic background for TTP in multiple families and is frequent among patients with congenital ADAMTS13 deficiency in Northern and Central European countries [22**]. Interestingly, several missense mutations can interact and alter the phenotype of ADAMTS13 deficiency [23**].

There are at least nine missense polymorphisms in the *ADAMTS13* gene. The Q448E mutation was shown not to affect the protease activity, whereas the P475S mutation decreased the activity [18]. This mutation is present in the Asian population but not in the white population [19,24,25]. It has been shown not to be a genetic risk factor for deep-vein thrombosis [26*].

Information regarding the wide variation of phenotypes in TTP patients with congenital ADAMTS13 deficiency has accumulated. Most patients with congenital ADAMTS13 deficiency had their first episode as newborn babies or in early infancy [10*]. After this period, the clinical manifestations of congenital ADAMTS13 deficiency vary from patient to patient, and patients are often incorrectly diagnosed with idiopathic thrombocytopenic purpura or Evans' syndrome during childhood. Seven women with congenital ADAMTS13 deficiency

who exhibited TTP at 5–6 months of pregnancy have been reported [27].

The factor V Leiden mutation is a well characterized and the most prevalent genetic risk factor for venous thrombosis. A previous study suggested that the factor V Leiden mutation may be a pathogenic risk factor in patients with thrombotic microangiopathy who have normal ADAMTS13 activity [28]. A recent study did not support the link between the factor V Leiden mutation and thrombotic microangiopathy [29].

Hemolytic uremic syndrome (HUS) is a thrombotic microangiopathy with manifestations of hemolytic anemia, thrombocytopenia, and renal impairment [1,8**,9**,30]. In most cases, typical HUS is triggered by Shiga toxin-producing *Escherichia coli* and manifests diarrhea (D+HUS). Atypical non-Shiga toxin-associated HUS is not associated with diarrhea (D–HUS), and deficiencies of complement factor H, membrane cofactor protein, and complement factor I have been reported in such atypical HUS [9**,31].

Epitopes of ADAMTS13 autoantibodies

Inhibitory autoantibodies for ADAMTS13 cause a deficiency of ADAMTS13 among patients with auto-immune TTP [3**,8**]. The prevalence of ADAMTS13 deficiency among patients with TTP varies from 13 to 100% depending on the criteria of the study. TTP may develop within 2–6 weeks after the antiplatelet agent ticlopidine is administered. TTP may develop in patients with HIV infection. No other apparent etiologies of inhibitory autoantibodies have been identified.

Several studies using recombinant ADAMTS13 and its truncated forms have identified the epitopes of

autoantibodies in patients with TTP. Many inhibitory autoantibodies recognized the spacer domain as the target epitope [32–34,35*]. Some reacted with the C-terminal CUB domains and the first thrombospondin type-1 (TSP-1) repeat [33]. Multiple B-cell clones producing antibodies directed against the spacer domain have been reported [36].

Assays of ADAMTS13 activity

ADAMTS13 assays such as multimer analysis by SDS/agarose-gel electrophoresis and residual collagen-binding analysis have been utilized for plasma ADAMTS13 activity in thrombotic microangiopathies and other pathophysiological conditions [2,4,6]. These assays quantify ADAMTS13 activity by measuring residual VWF multimers or their activity, suggesting that more accurate and simpler assays are in demand.

New assays using VWF73 peptide as the ADAMTS13 substrate

In 2004, we identified a 73-amino acid sequence spanning residues D1596–R1668 of the VWF A2 domain, VWF73, as the minimum region for ADAMTS13 cleavage [37]. A shorter peptide, VWF64, from D1596 to R1659, was not a good substrate for ADAMTS13. Since the development of VWF73 as the substrate for ADAMTS13, several new assays based on the VWF73 sequence have been developed [37–39,40*–43*]. So far, seven assays have been published for the VWF73-based measurements of ADAMTS13 activity. The characteristics of these assays are summarized in Table 1 [37–39,40*–43*]. The assays have the advantages of being simple, rapid, accurate, and quantitative. They do not require denaturing conditions; therefore, the incubation time of the substrates and plasma samples is reduced to less than 1 h. They give rise to quantitative measures. In addition, most of the assays are compatible with the 96-well

microplates that clinical-laboratory workers are familiar with, so they have the potential to be widely used in clinical settings.

Of the seven assays, FRETS-VWF73, a fluorogenic substrate for ADAMTS13, is well characterized. The advantage of using FRETS-VWF73 is that the ADAMTS13 activity can be determined by the initial velocity of the increase in fluorescence. Therefore, the assay is highly quantitative. ADAMTS13 cleaves VWF with a $K_m$app of 3.7 ± 1.4 μg/ml or 15 nM in VWF subunits, which is comparable with the plasma VWF concentration of 5–10 μg/ml, and with a value for k_{cat} of ~ 0.83 min^{-1} [44*]. ADAMTS13 cleaves FRETS-VWF73 with a $K_m$app of 3.2 ± 1.1 μM and a k_{cat} of ~ 58 min^{-1}. Thus, the affinity of ADAMTS13 to FRETS-VWF73 was decreased ~ 200-fold compared with VWF, but the catalytic efficiency was ~ 70-fold greater than VWF. Therefore, ADAMTS13 cleaves VWF and FRETS-VWF73 with roughly comparable catalytic efficiencies of 55 and 18 μM^{-1} min^{-1}, respectively [44*].

FRETS-VWF73 was evaluated by three different research groups [45–47]. Although the definitive evaluation remains to be determined in a large cohort of patients diagnosed with acquired or congenital TTP, ADAMTS13 activity determined by FRETS-VWF73 assay was in good accordance with that measured by conventional assays. FRETS-VWF73 is now commercially available (Table 2).

There may be limitations of the VWF73-based ADAMTS13 assays. VWF73, a small fragment of the A2 domain of VWF, may lack additional sites on VWF that interact with ADAMTS13. The A1 domain of VWF binds cofactors such as platelet glycoprotein Ib and heparin to regulate cleavage [48], and the A3 domain may be a docking site for ADAMTS13 [49]. VWF73 lacks

Table 1 VWF73-based ADAMTS13 activity assays

Substrate	Principle	Reference
GST–VWF73 fusion protein with the C-terminal 6×His tag	Western-blot detection using anti-GST antibody	[37]
FRETS-VWF73, synthetic VWF73 peptide with a fluorophore at the P7 position and a quencher at the P5' position	Fluorescence resonance energy transfer, initial-velocity method	[39]
Immobilized GST–VWF73 fusion protein with the C-terminal 6×His tag	Enzyme immunoassay, the amount of 6×His remaining was assayed with anti-6×His IgG conjugated with HRP, end point method	[38]
Immobilized His- and biotin-labeled VWF73 conjugated with HRP	Enzyme-linked assay, endpoint method	[40*]
Immobilized GST–VWF73 fusion protein with the C-terminal 6×His tag	Mass-spectrometry analysis of the products, endpoint method	[41*]
Immobilized GST–VWF73 fusion protein with the C-terminal 6×His tag	Enzyme immunoassay, the amount of products were assayed with anti-N10 mAbs conjugated with HRP, endpoint method	[42*]
Recombinant 6×His-tagged VWF73 peptide labeled with fluorescein at both the P7 and P6' positions	Fluorescence resonance energy transfer, initial-velocity method	[43*]

GST, glutathione-S-transferase; HRP, horseradish peroxidase; mAb, monoclonal antibody; VWF73, 73 amino acid residues of von Willebrand factor (VWF) from D1596 to R1668.

Table 2 Commercially available kits for assaying ADAMTS13 activity and antigen

Kit	Maker/supplier	Objectives	Time
FRETS-VWF73	Peptide Institute, Peptides International	Activity	1 h
ATS-13 ADAMTS-13 Activity	GTI	Activity	30 min
ADAMTS13 ELISA kit	Mitsubishi Kagaku Iatron	Antigen	3.5 h
ADAMTS13 activity ELISA kit	KAINOS LABORATORIES	Activity	3.5 h
TECHNOZYM ADAMTS-13	Technoclone GmbH	Activity/antigen	2.5 h/4 h
TECHNOZYM ADAMTS-13 INH	Technoclone GmbH	Autoantibody	2.5 h
ACTIFLUOR ADAMTS13 Activity Assay kit	American Diagnostica	Activity	
IMUBIND ADAMTS13 ELISA	American Diagnostica	Antigen	5 h
IMUBIND ADAMTS13/fXI Complex ELISA	American Diagnostica	ADAMTS13/FXI complex	4 h
IMUBIND ADAMTS13 Autoantibody ELISA	American Diagnostica	Autoantibody	4 h

these domains. Therefore, if enzyme defects in patients with TTP affect the ADAMTS13-binding site for these domains, cleavage of VWF73 will not reflect these defects.

Measurements of ADAMTS13 autoantibodies

Autoantibodies neutralizing ADAMTS13 activity are a major cause of acquired TTP. The presence or absence of inhibitory autoantibodies is important in discriminating acquired from congenital TTP. An inhibitor assay is generally carried out using mixtures of heat-inactivated plasma from patients and normal plasma at a 1:1 dilution or several dilutions. Assays for ADAMTS13 activity so far developed, including VWF73-based assays, are compatible for the inhibitor assay. It should be noted that nonneutralizing autoantibodies may reduce the circulating ADAMTS13 levels by antibody-mediated clearance.

ELISA has been developed to detect autoantibodies against ADAMTS13. In this process, immobilized ADAMTS13 in the plate wells captures both inhibitory and noninhibitory autoantibodies in plasma samples; then secondary detection antibodies, such as goat antihuman IgG or IgM antibodies labeled with horseradish peroxidase, are added and the levels of ADAMTS13-binding IgGs are determined [50]. Using this assay, low titers of IgG antibodies were detected in four out of 111 healthy control donors who lacked anti-ADAMTS13 inhibitory activity by inhibitor assays. IgG autoantibodies were found in 97% of untreated patients with acute acquired thrombotic microangiopathies who had plasma ADAMTS13 activity levels below 10% [51]. This assay was more sensitive than the standard functional inhibitor assay for detecting autoantibodies against ADAMTS13. The ELISA kit utilizing this principle is now commercially available (Table 2), and has been validated to be useful [52].

Antigen assays for plasma ADAMTS13

ELISA for measuring plasma ADAMTS13 antigen levels has also been developed by several research groups. ADAMTS13 antigen ELISA kits are also commercially available (Table 2).

Healthy plasma ADAMTS13 levels

The ELISA assay to detect plasma ADAMTS13 levels can estimate the plasma ADAMTS13 concentration when the ADAMTS13 standard can be obtained from recombinant full-length ADAMTS13 protein. The ADAMTS13 antigen concentration in normal human plasma pooled from white donors was $1.03 \pm 0.15 \,\mu g/ml$ of plasma [53•]. Interestingly, normal Chinese donors have significantly lower antigen levels ($0.62 \pm 0.13 \,\mu g/ml$). In another study of 99 healthy Austrian donors, the median plasma ADAMTS13 level was $1.08 \,\mu g/ml$ using recombinant ADAMTS13 as the standard [54•]. The plasma ADAMTS13 level in Japanese donors was reported to be 0.82 ± 0.15 and $0.70 \pm 0.13 \,\mu g/ml$ using two different ELISA systems when recombinant ADAMTS13 was used as the standard [55•].

Phenotype of mice lacking *Adamts13* gene

The mouse is a promising animal model for seeking genetic or environmental susceptibility factor(s) for a certain disease phenotype. Two types of mouse *Adamts13* cDNA have been isolated and characterized [56]. cDNA isolated from the 129/Sv strain showed a domain organization identical to the human one. The other cDNA lacked the C-terminal two TSP-1 motifs and two CUB domains due to the insertion of an intracisternal A particle retrotransposon in intron 23, which creates a premature stop codon. Both recombinant proteins showed VWF-cleaving activity *in vitro*.

Mice lacking the *Adamts13* gene have been recently developed by us and another group [57,58••,59••]. We generated mice lacking the *Adamts13* gene by replacing exons 3–6 encoding the catalytic domain by a neomycin-resistant cassette and analyzed phenotypes on a 129/Sv genetic background of the ADAMTS13-deficient mice [58••]. The ADAMTS13-deficient mice were born in the expected Mendelian distribution. Plasma from homozygous mice showed no ADAMTS13 activity. The mice were viable and fertile. Hematologic and histologic examinations failed to detect any evidence of thrombocytopenia, hemolytic anemia, or microvascular thrombosis. However, ULVWF multimers were observed in the plasma of homozygotes. Thrombus formation on immobilized

collagen under flow was significantly elevated in homozygotes in comparison with wild-type mice. Thrombocytopenia was more severely induced in homozygotes than in wild-type mice after intravenous injection of a mixture of collagen and epinephrine. Therefore, a complete lack of ADAMTS13 in mice caused a prothrombotic state, but it alone was not sufficient to cause TTP. Factors in addition to ADAMTS13 deficiency may be necessary for development of TTP.

Mice lacking the *Adamts13* gene have also been generated with replacement of exons 1–6 by a neomycin cassette [57]. The ADAMTS13-deficient mice were born in the expected Mendelian distribution and homozygous mice were viable and fertile. When the VWF multimer analysis was examined in the ADAMTS13-deficient mice on a mixed-strain C57BL/6J and 129X1/SvJ genetic background, the multimers of wild-type mice and ADAMTS13-deficient mice were indistinguishable. However, the ADAMTS13-deficient mice, after two generations of backcrossing to the CASA/Rk strain (a mouse strain with elevated plasma VWF), showed ULVWF multimers compared with wild-type littermates. Mice with a mixed CASA/Rk background showed a significant decrease in platelet count and a fraction of the deficient mice exhibited severe thrombocytopenia and significantly decreased survival compared with wild-type or heterozygous controls. These mice showed a TTP-like phenotype such as severe microangiopathic changes in the peripheral blood and VWF-rich and fibrin-poor hyaline thrombi in the small vessels. Deficient mice showed prolongation of VWF-mediated platelet-endothelial interactions, indicating that ADAMTS13 regulates VWF-mediated platelet adhesion *in vivo*. When Shiga toxin was infused intravenously, TTP-like symptoms were observed in ADAMTS13-deficient mice with a mixed CASA/Rk background, but not in mice with a mixed C57BL/6J background. Shiga toxin is known to induce HUS through endothelial dysfunction. Thus, TTP can be induced in ADAMTS13-deficient mice by agents causing endothelial dysfunction. This strain-specific difference of TTP pathogenesis in mice may indicate the contribution of additional genetic factors.

Further characterizations of events *in vivo* in ADAMTS13-deficient mice on a mixed-strain C57BL/6J and 129X1/SvJ genetic background have been examined [59**]. When the microvenule endothelium in ADAMTS13-deficient mice was activated with calcium ionophore, ULVWF multimers were secreted from Weibel–Palade body, and platelet aggregation resulting in spontaneous thrombus formation was observed using intravital microscopy. In wild-type littermates, platelet strings and very small aggregation could be seen attached to the endothelium, but thrombi did not form. A ferric chloride injury model on arterioles

exhibited that ADAMTS13 downregulates both platelet adhesion to the exposed subendothelium and thrombus formation. Infusion of recombinant ADAMTS13 into ADAMTS13-deficient or wild-type mice inhibited similar thrombus growth. These findings revealed that ADAMTS13 is a natural anticoagulant.

Conclusion

A highly accurate and quantitative assay method for measuring ADAMTS13 activity has been developed. These assays are now commercially available and will be widely utilized for a clinical diagnosis in patients with microangiopathy to discriminate TTP from HUS or other thrombocytopenia. Mice lacking the *Adamts13* gene were viable and fertile. They did not show the TTP-like phenotype such as spontaneous thrombocytopenia, but intensive analyses revealed that they were prothrombotic. They are useful models to reveal how ADAMTS13 deficiency interacts with other genetic and environmental factors.

Acknowledgements

References and recommended reading

Papers of particular interest, published within the annual period of review, have been highlighted as:
• of special interest
•• of outstanding interest
Additional references related to this topic can also be found in the Current World Literature section in this issue (p. 296).

1 Moake JL. Thrombotic microangiopathies. N Engl J Med 2002; 347:589–600.

2 Sadler JE, Moake JL, Miyata T, George JN. Recent advances in thrombotic thrombocytopenic purpura. Hematology Am Soc Hematol Edu Program 2004; 407–423.

3 Sadler JE. Thrombotic thrombocytopenic purpura: a moving target. Hematol-
•• ogy Am Soc Hematol Edu Program 2006; 415–420.
This review integrates the current knowledge about ADAMTS13 into a model of TTP.

4 Miyata T, Kokame K, Banno F. Measurement of ADAMTS13 activity and inhibitors. Curr Opin Hematol 2005; 12:384–389.

5 Levy GG, Motto DG, Ginsburg D. ADAMTS13 turns 3. Blood 2005; 106: 11–17.

6 Shelat SG, Ai J, Zheng XL. Molecular biology of ADAMTS13 and diagnostic utility of ADAMTS13 proteolytic activity and inhibitor assays. Semin Thromb Hemost 2005; 31:659–672.

7 Bowen DJ, Collins PW. Insights into von Willebrand factor proteolysis: clinical
• implications. Br J Haematol 2006; 133:457–467.
This review summarizes the clinical implications of VWF proteolysis, especially in the ABO blood group and VWF polymorphism.

8 Tsai HM. Current concepts in thrombotic thrombocytopenic purpura. Annu
•• Rev Med 2006; 57:419–436.
This review summarizes recent advances in autoimmune TTP and hereditary TTP.

9 Tsai HM. The molecular biology of thrombotic microangiopathy. Kidney Int
•• 2006; 70:16–23.
This review deals with TTP and atypical HUS.

10 Loirat C, Veyradier A, Girma JP, et al. Thrombotic thrombocytopenic purpura
• associated with von Willebrand factor-cleaving protease (ADAMTS13) deficiency in children. Semin Thromb Hemost 2006; 32:90–97.
The review deals with children with TTP.

11 Uemura M, Tatsumi K, Matsumoto M, et al. Localization of ADAMTS13 to the stellate cells of human liver. Blood 2005; 106:922–924.

12 Zhou W, Inada M, Lee TP, et al. ADAMTS13 is expressed in hepatic stellate cells. Lab Invest 2005; 85:780–788.

13 Suzuki M, Murata M, Matsubara Y, et al. Detection of von Willebrand factor-cleaving protease (ADAMTS-13) in human platelets. Biochem Biophys Res Commun 2004; 313:212–216.

14 Liu L, Choi H, Bernardo A, et al. Platelet-derived VWF-cleaving metallopro- tease ADAMTS-13. J Thromb Haemost 2005; 3:2536–2544.

15 Turner N, Nolasco L, Tao Z, et al. Human endothelial cells synthesize and
• release ADAMTS-13. J Thromb Haemost 2006; 4:1396–1404.
The authors reported human endothelial cells as ADAMTS13-producing cells.

16 Shang D, Zheng XW, Niiya M, Zheng XL. Apical sorting of ADAMTS13 in
•• vascular endothelial cells and Madin-Darby canine kidney cells depends on the CUB domains and their association with lipid rafts. Blood 2006; 108: 2207–2215.
This study identified C-terminal CUB domains as the apical sorting signal of the ADAMTS13 molecule.

17 Levy GG, Nichols WC, Lian EC, et al. Mutations in a member of the ADAMTS gene family cause thrombotic thrombocytopenic purpura. Nature 2001; 413:488–494.

18 Kokame K, Matsumoto M, Soejima K, et al. Mutations and common polymorphisms in ADAMTS13 gene responsible for von Willebrand factor- cleaving protease activity. Proc Natl Acad Sci USA 2002; 99:11902–11907.

19 Kokame K, Miyata T. Genetic defects leading to hereditary thrombotic thrombocytopenic purpura. Semin Hematol 2004; 41:34–40.

20 Donadelli R, Banterla F, Galbusera M, et al. In-vitro and in-vivo consequences
• of mutations in the von Willebrand factor cleaving protease ADAMTS13 in thrombotic thrombocytopenic purpura. Thromb Haemost 2006; 96:454– 464.
The authors reported ADAMTS13 mutations and polymorphisms on behalf of the International Registry of Recurrent and Familial HUS/TTP.

21 Peyvandi F, Lavoretano S, Palla R, et al. Mechanisms of the interaction between two ADAMTS13 gene mutations leading to severe deficiency of enzymatic activity. Hum Mutat 2006; 27:330–336.

22 Schneppenheim R, Kremer Hovinga JA, Becker T, et al. A common origin of
•• the 4143insA ADAMTS13 mutation. Thromb Haemost 2006; 96:3–6.
The authors identified the 4143insA mutation in the ADAMTS13 gene as a common origin for ADAMTS13 deficiency in European lineages.

23 Plaimauer B, Fuhrmann J, Mohr G, et al. Modulation of ADAMTS13 secretion
•• and specific activity by a combination of common amino acid polymorphisms and a missense mutation. Blood 2006; 107:118–125.
Two patients with congenital TTP carried five missense mutations that can interact with each other, thereby altering the phenotype of ADAMTS13 deficiency.

24 Ruan C, Dai L, Su J, et al. The frequency of P475S polymorphism in von Willebrand factor-cleaving protease in the Chinese population and its relevance to arterial thrombotic disorders. Thromb Haemost 2004; 91: 1257–1258.

25 Bongers TN, De Maat MP, Dippel DW, et al. Absence of Pro475Ser polymorphism in ADAMTS-13 in Caucasians. J Thromb Haemost 2005; 3: 805.

26 Kimura R, Honda S, Kawasaki T, et al. Protein S-K196E mutation as a genetic
• risk factor for deep vein thrombosis in Japanese patients. Blood 2006; 107:1737–1738.
The P475S mutation in ADAMTS13 was not a risk factor for deep-vein thrombosis.

27 Matsuyama T, Matsumoto M, Kato S, et al. Upshaw-Schulman syndrome: a masqueraded thrombocytopenia during pregnancy. Blood 2005; 106: ab- stract no. 2644.

28 Raife TJ, Lentz SR, Atkinson BS, et al. Factor V Leiden: a genetic risk factor for thrombotic microangiopathy in patients with normal von Willebrand factor-cleaving protease activity. Blood 2002; 99:437–442.

29 Krieg S, Studt JD, Sulzer I, et al. Is factor V Leiden a risk factor for thrombotic microangiopathies without severe ADAMTS 13 deficiency? Thromb Haemost 2005; 94:1186–1189.

30 Shibagaki Y, Fujita T. Thrombotic microangiopathy in malignant hypertension and hemolytic uremic syndrome (HUS)/thrombotic thrombocytopenic purpura (TTP): can we differentiate one from the other? Hypertens Res 2005; 28:89–95.

31 Caprioli J, Noris M, Brioschi S, et al. Genetics of HUS: the impact of MCP, CFH, and IF mutations on clinical presentation, response to treatment, and outcome. Blood 2006; 108:1267–1279.

32 Soejima K, Matsumoto M, Kokame K, et al. ADAMTS-13 cysteine-rich/spacer domains are functionally essential for von Willebrand factor cleavage. Blood 2003; 102:3232–3237.

33 Klaus C, Plaimauer B, Studt JD, et al. Epitope mapping of ADAMTS13 autoantibodies in acquired thrombotic thrombocytopenic purpura. Blood 2004; 103:4514–4519.

34 Luken BM, Turenhout EA, Hulstein JJ, et al. The spacer domain of ADAMTS13 contains a major binding site for antibodies in patients with thrombotic thrombocytopenic purpura. Thromb Haemost 2005; 93:267–274.

35 Luken BM, Turenhout EA, Kaijen PH, et al. Amino acid regions 572-579 and
• 657-666 of the spacer domain of ADAMTS13 provide a common antigenic core required for binding of antibodies in patients with acquired TTP. Thromb Haemost 2006; 96:295–301.
The authors reported the spacer domain of ADAMTS13 to be the autoantibody target.

36 Luken BM, Kaijen PH, Turenhout EA, et al. Multiple B-cell clones producing antibodies directed to the spacer and disintegrin/thrombospondin type-1 repeat 1 (TSP1) of ADAMTS13 in a patient with acquired thrombotic thrombocytopenic purpura. J Thromb Haemost 2006; 4:2355–2364.

37 Kokame K, Matsumoto M, Fujimura Y, Miyata T. VWF73, a region from D1596 to R1668 of von Willebrand factor, provides a minimal substrate for ADAMTS- 13. Blood 2004; 103:607–612.

38 Zhou W, Tsai HM. An enzyme immunoassay of ADAMTS13 distinguishes patients with thrombotic thrombocytopenic purpura from normal indivi- duals and carriers of ADAMTS13 mutations. Thromb Haemost 2004; 91: 806–811.

39 Kokame K, Nobe Y, Kokubo Y, et al. FRETS-VWF73, a first fluorogenic substrate for ADAMTS13 assay. Br J Haematol 2005; 129:93–100.

40 Wu JJ, Fujikawa K, Lian EC, et al. A rapid enzyme-linked assay for ADAMTS-13.
• J Thromb Haemost 2006; 4:129–136.
The authors developed a VWF73-based horseradish peroxidase-labeled substrate to assay for ADAMTS13 activity.

41 Jin M, Cataland S, Bissell M, Wu HM. A rapid test for the diagnosis of thrombotic
• thrombocytopenic purpura using surface enhanced laser desorption/ionization time-of-flight (SELDI-TOF)-mass spectrometry. J Thromb Haemost 2006; 4: 333–338.
The authors developed an accurate and quantitative ADAMTS13 assay using mass spectrometry.

42 Kato S, Matsumoto M, Matsuyama T, et al. Novel monoclonal antibody-based
• enzyme immunoassay for determining plasma levels of ADAMTS13 activity. Transfusion 2006; 46:1444–1452.
The authors developed a quantitative ADAMTS13 activity assay using a mono- clonal antibody that specifically recognizes the cleavage of VWF73.

43 Zhang L, Lawson HL, Harish VC, et al. Creation of a recombinant peptide
• substrate for fluorescence resonance energy transfer-based protease assays. Anal Biochem 2006; 358:298–300.
The authors developed a recombinant substrate for an ADAMTS13 assay based on fluorescence resonance energy transfer.

44 Anderson PJ, Kokame K, Sadler JE. Zinc and calcium ions cooperatively
• modulate ADAMTS13 activity. J Biol Chem 2006; 281:850–857.
The enzyme-kinetic parameters of ADAMTS13 for the natural substrate VWF and the synthetic substrate FRETS-VWF73 are reported here.

45 Groot E, Hulstein JJ, Rison CN, et al. FRETS-VWF73: a rapid and predictive tool for thrombotic thrombocytopenic purpura. J Thromb Haemost 2006; 4:698–699.

46 Kremer Hovinga JA, Mottini M, Lammle B. Measurement of ADAMTS-13 activity in plasma by the FRETS-VWF73 assay: comparison with other assay methods. J Thromb Haemost 2006; 4:1146–1148.

47 Mahdian R, Rayes J, Girma JP, et al. Comparison of FRETS-VWF73 to full-length VWF as a substrate for ADAMTS13 activity measurement in human plasma samples. Thromb Haemost 2006; 95:1049–1051.

48 Nishio K, Anderson PJ, Zheng XL, Sadler JE. Binding of platelet glycoprotein Ibα to von Willebrand factor domain A1 stimulates the cleavage of the adjacent domain A2 by ADAMTS13. Proc Natl Acad Sci USA 2004; 101: 10578–10583.

49 Dong JF, Moake JL, Bernardo A, et al. ADAMTS-13 metalloprotease interacts with the endothelial cell-derived ultra-large von Willebrand factor. J Biol Chem 2003; 278:29633–29639.

50 Scheiflinger F, Knobl P, Trattner B, et al. Nonneutralizing IgM and IgG antibodies to von Willebrand factor-cleaving protease (ADAMTS-13) in a patient with thrombotic thrombocytopenic purpura. Blood 2003; 102: 3241–3243.

51 Rieger M, Mannucci PM, Kremer Hovinga JA, et al. ADAMTS13 autoantibodies in patients with thrombotic microangiopathies and other immunomediated diseases. Blood 2005; 106:1262–1267.

52 Tsai HM, Raoufi M, Zhou W, et al. ADAMTS13-binding IgG are present in patients with thrombotic thrombocytopenic purpura. Thromb Haemost 2006; 95:886–892.

53 Feys HB, Liu F, Dong N, *et al.* ADAMTS-13 plasma level determination
• uncovers antigen absence in acquired thrombotic thrombocytopenic purpura
and ethnic differences. J Thromb Haemost 2006; 4:955–962.
This study reported that Chinese have significantly lower ADAMTS13 antigen
levels.

54 Rieger M, Ferrari S, Kremer Hovinga JA, *et al.* Relation between ADAMTS13
• activity and ADAMTS13 antigen levels in healthy donors and patients with
thrombotic microangiopathies (TMA). Thromb Haemost 2006; 95:212–
220.
These workers established an ELISA assay for ADAMTS13 antigen levels and
reported the median plasma ADAMTS13 level to be 1.08 μg/ml.

55 Soejima K, Nakamura H, Hirashima M, *et al.* Analysis on the molecular species
• and concentration of circulating ADAMTS13 in blood. J Biochem (Tokyo)
2006; 139:147–154.
In this study the plasma ADAMTS13 concentration was reported as 0.5–1 μg/ml
and the extinction coefficient of recombinant ADAMTS13 was 1.7.

56 Banno F, Kaminaka K, Soejima K, *et al.* Identification of strain-specific variants
of mouse *Adamts13* gene encoding von Willebrand factor-cleaving protease.
J Biol Chem 2004; 279:30896–30903.

57 Motto DG, Chauhan AK, Zhu G, *et al.* Shigatoxin triggers thrombotic throm-
bocytopenic purpura in genetically susceptible ADAMTS13-deficient mice.
J Clin Invest 2005; 115:2752–2761.

58 Banno F, Kokame K, Okuda T, *et al.* Complete deficiency in ADAMTS13 is
•• prothrombotic, but it alone is not sufficient to cause thrombotic thrombocy-
topenic purpura. Blood 2006; 107:3161–3166.
The authors produced ADAMTS13-deficient mice that exhibited thrombocytopenia
by the intravenous injection of collagen.

59 Chauhan AK, Motto DG, Lamb CB, *et al.* Systemic antithrombotic effects of
•• ADAMTS13. J Exp Med 2006; 203:767–776.
The authors demonstrated spontaneous thrombus formation in activated microve-
nules of *Adamts13*-deficient mice by intravital microscopy.

ARTICLE

Differential Expression Patterns of NDRG Family Proteins in the Central Nervous System

Tomohiko Okuda, Koichi Kokame, and Toshiyuki Miyata

National Cardiovascular Center Research Institute, Osaka, Japan

SUMMARY The N-myc downstream-regulated gene (NDRG) family consists of four proteins: NDRG1, NDRG2, NDRG3, and NDRG4 in mammals. NDRG1 has been thoroughly studied as an intracellular protein associated with stress response, cell growth, and differentiation. A nonsense mutation in the NDRG1 gene causes hereditary motor and sensory neuropathy, Charcot–Marie–Tooth disease type 4D. We previously generated *Ndrg1*-deficient mice and found that they exhibited peripheral nerve degeneration caused by severe demyelination, but that the complicated motor abilities were retained. These results implied that other NDRG family proteins may compensate for the NDRG1 deficiency in the central nervous system. In this study we raised specific antibodies against each member of the NDRG protein family and examined their cellular expression patterns in the mouse brain. In the cerebrum, NDRG1 and NDRG2 were localized in oligodendrocytes and astrocytes, respectively, whereas NDRG3 and NDRG4 were ubiquitous. In the cerebellum, NDRG1 and NDRG4 were localized in Purkinje cells and NDRG2 in Bergmann glial cells. NDRG3 was detected in the nuclei in most cells. These expression patterns demonstrated the cell type-specific and ubiquitous localization of the NDRG family proteins. Each NDRG may play a partially redundant role in specific cells in the brain. (J Histochem Cytochem 56:175–182, 2008)

THE N-myc downstream-regulated gene (NDRG) family consists of four proteins: NDRG1, NDRG2, NDRG3, and NDRG4 in mammals. They are intracellular proteins of 340 to 394 amino acids and share 53 to 65% sequence identities to each other (Okuda and Kondoh 1999; Zhou et al. 2001; Qu et al. 2002). Among this family of proteins, NDRG1 has been thoroughly studied as an inducible protein by a number of stress and pathological conditions (Kovacevic and Richardson 2006). *NDRG1* was first identified as a stress stimuli-induced gene (Kokame et al. 1996; Zhou et al. 1998). It was also reported as a downregulated gene in tumors (van Belzen et al. 1997), regulated by p53 (Kurdistani et al. 1998; Stein et al. 2004), associated with the differentiation and malignant states of cancers (Piquemal et al. 1999; Xu et al. 1999; Guan et al. 2000; Bandyopadhyay et al. 2003), and regulated by *N-myc* (Shimono et al. 1999).

NDRG1 is the gene responsible for Charcot–Marie–Tooth disease type 4D (CMT4D), also called hereditary motor and sensory neuropathy-Lom (Kalaydjieva et al. 1996,2000). Patients exhibit early-onset peripheral neuropathy, which progresses in adulthood to severe disability characterized by muscle weakness, sensory loss, and neural deafness. Diseases caused by deficiency of NDRG2, NDRG3, or NDRG4 have not yet been identified. Although studies about the NDRG family proteins have been accumulating, their molecular functions are still elusive.

To clarify the physiological roles of NDRG1, we generated *Ndrg1*-deficient mice and analyzed their phenotypes (Okuda et al. 2004). They exhibited a progressive demyelinating disorder of the peripheral nerves. Sporadic demyelination began by 5 weeks of age in the sciatic nerve, whereas the proliferation of Schwann cells and initial myelination were normal for 2 weeks after birth. In wild-type mice, NDRG1 was abundantly expressed in the cytoplasm of Schwann cells rather than in the myelin sheaths. Therefore, NDRG1 deficiency leads to autonomous dysfunction of Schwann cells, resulting in demyelination in peripheral nerves. This suggests that NDRG1 is essential for the maintenance of

myelin sheaths in peripheral nerves. In contrast to muscle weakness caused by peripheral nerve degeneration, the complicated motor abilities in *Ndrg1*-deficient mice were relatively retained. These results suggest that functional compensation for NDRG1 deficiency may exist in the central nervous system (CNS).

Transcripts of NDRG1, NDRG2, NDRG3, and NDRG4 have been detected in the brain (Zhou et al. 2001; Okuda et al. 2004). In the present study we raised specific antibodies against each member of NDRGs and examined their expression patterns in the mouse CNS by immunohistochemical analysis. We found the cell type-specific and ubiquitous localization of NDRGs.

Materials and Methods

Animals

Adult male mice (C57BL/6 Cr Slc) aged 8 to 12 weeks (Japan SLC Inc.; Hamamatsu, Japan) were used in this study. Adult or 4-week-old *Ndrg1*-deficient male mice (Okuda et al. 2004) were also used. Mice were bred at a controlled temperature (22C) and lighting (lights on at 8 AM and off at 8 PM) for at least 1 week. Animal experiments were conducted in accordance with the guidelines for the care and use of experimental animals of the National Cardiovascular Center in Japan.

Antibodies and Vectors

Rabbit polyclonal anti-human NDRG1 and anti-human NDRG4 antibodies were raised against bacterial recombinant glutathione S-transferase-fusion proteins of NDRG1 and NDRG4, respectively, and purified by the fusion protein-immobilized affinity column chromatography (Agarwala et al. 2000; Zhou et al. 2001). Rabbit polyclonal anti-NDRG2 and anti-NDRG3 antibodies were raised against the following synthetic peptides conjugated with keyhole limpet hemocyanin and purified by peptide-immobilized affinity column chromatography: Q^{351}SSESGTLPSGPPGH^{365} for mouse NDRG2 and F^{343}SRSVTSNQSDGTQE^{357} for mouse NDRG3. The mouse monoclonal anti-2′,3′-cyclic nucleotide 3′-phosphodiesterase (CNPase) antibody (clone 11-5B) was purchased from Sigma-Aldrich (St Louis, MO). Mouse monoclonal anti-glial fibrillary acidic protein (GFAP) antibody and mouse monoclonal anti-neuronal nuclei (NeuN) antibody were purchased from Chemicon (Temecula, CA).

Expression vectors for the green fluorescent protein (GFP)-fusion proteins of mouse NDRG1, NDRG2, NDRG3, and NDRG4 were constructed with the pEGFP-N1 vector (Clontech; Mountain View, CA). COS-1 cells were transfected with these vectors using the FuGENE6 transfection reagent (Roche Diagnostics; Indianapolis, IN). Two days later, cells were collected and lysed with lysis buffer (10 mM Tris–HCl, 2 mM EDTA, 50 mM dithiothreitol, 2% SDS, 6% glycerol, pH 6.8).

Western Blotting Analysis

The excised whole brain was homogenized in the lysis buffer. Protein lysates were subjected to SDS-PAGE (10–20% gradient gel; Daiichi Pure Chemicals, Tokyo, Japan) and transferred to a polyvinylidene difluoride membrane (Bio-Rad; Hercules, CA). An equal amount of loading of the protein samples was confirmed by using the RC DC protein assay kit (Bio-Rad). After blocking with 3% skim milk in PBS with 0.05% Tween-20, the membrane was incubated with 0.5-μg/ml antibodies and then with a 1:1000 dilution of peroxidase-conjugated goat anti-rabbit IgG (Zymed; South San Francisco, CA). Chemiluminescent signals were developed using Western Lightning Chemiluminescence Reagent Plus (PerkinElmer Life Sciences; Wellesley, MA) and detected by an image analyzer LAS-1000plus (Fuji Film; Tokyo, Japan).

Histological Analyses

Mice (8–12 weeks old) were anesthetized with Nembutal (Abbott Laboratories; North Chicago, IL) and perfused with ice-cold 4% paraformaldehyde in PBS. Brain was then excised and fixed in 4% paraformaldehyde in PBS overnight at 4C. For light microscopy, specimens were embedded in paraffin by standard procedures. Four-μm-thick paraffin sections were stained with hematoxylin–eosin or luxol–fast blue (Klüver-Barrera staining). Slides were examined with the Axioplan 2 microscope (Carl Zeiss; Oberkochen, Germany). For immunofluorescence microscopy, 4% paraformaldehyde-fixed brain specimens were washed with PBS at 4C, immersed in a 10–20% sucrose concentration ascending series in PBS overnight at 4C, and embedded in optimal cutting temperature compound (OCT; Sakura Finetek Torrance, CA) on dry ice. Five-μm-thick frozen sections were cut by a cryostat microtome and washed with PBS. After blocking with 10% normal goat serum for 30 min at room temperature, sections were incubated with a 1 μg/ml solution of each anti-NDRG antibody, a 1:200 dilution of anti-CNPase, a 1:200 dilution of anti-GFAP, and a 1:200 dilution of anti-NeuN overnight at 4C. They were then incubated with a 1:200 dilution of AlexaFluor 488-conjugated anti-rabbit IgG antibody and/or a 1:200 dilution of AlexaFluor 546-conjugated anti-mouse IgG antibody (Invitrogen; Carlsbad, CA) for 1 hr at room temperature. Fluorescence was detected with the Axiovert 200 microscope and photographed with the AxioCam (Carl Zeiss). For negative controls of immunostaining, normal rabbit IgG was used as a primary antibody instead of as a specific antibody.

Results

Raising Specific Antibodies Against the NDRG Family Proteins

We previously raised antibodies against human NDRG1 and NDRG4 (Agarwala et al. 2000; Zhou et al. 2001). Western blotting analysis showed that anti-NDRG1 and anti-NDRG4 specifically reacted with recombinant mouse NDRG1-GFP and NDRG4-GFP, respectively, and that anti-NDRG1 faintly cross-reacted with recombinant mouse NDRG3-GFP (Figure 1). In addition to these antibodies, in the present study we raised antibodies against mouse NDRG2 and NDRG3. They specifically reacted with recombinant mouse NDRG2-GFP and NDRG3-GFP, respectively, without any cross-reactions (Figure 1).
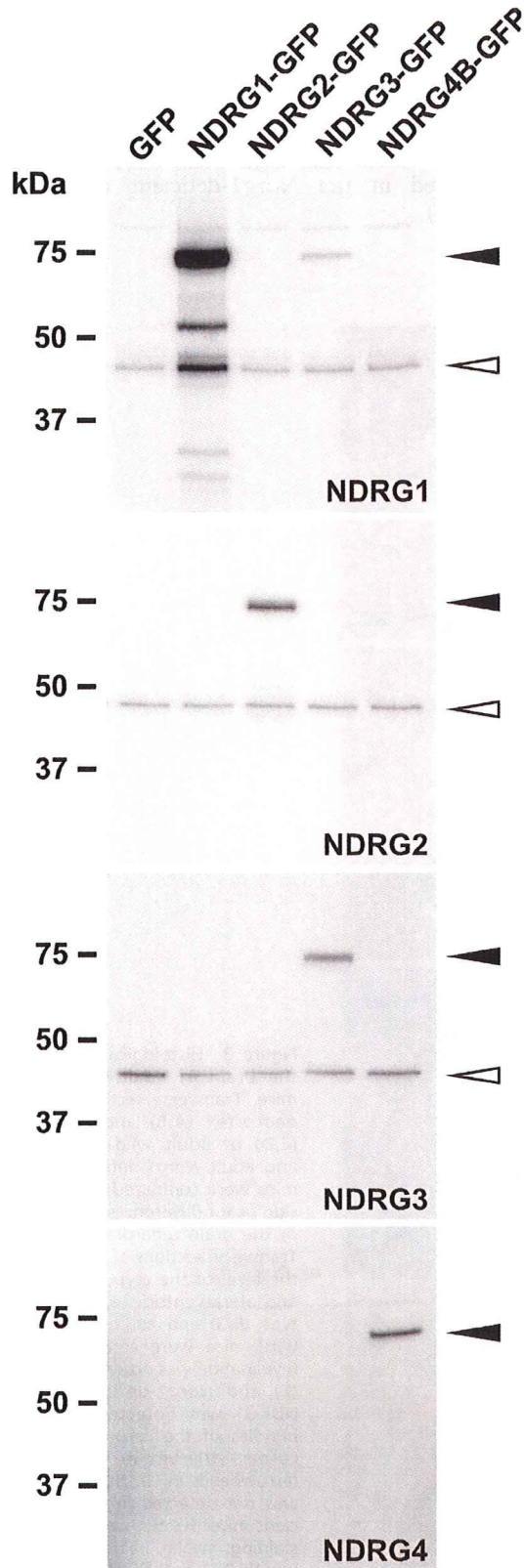
Figure 1 Antibody specificity against NDRG family proteins. Lysates of COS-1 cells transfected with green fluorescent protein (GFP) or mouse NDRG–GFP vectors were analyzed by Western blotting. Each antibody specifically reacted with respective NDRG–GFP fusion proteins (closed arrowheads). Bands indicated by open arrowheads were endogenous NDRG proteins. Each lane contained 5 μg of total protein.

Using these antibodies, we detected all the NDRG family proteins in the brain of wild-type mice aged 4 and 12 weeks (Figure 2). Expression amounts of NDRG2, NDRG3, and NDRG4 proteins were not affected in the brain of *Ndrg1*-deficient mice, suggesting that the loss of NDRG1 did not affect expression levels of the other NDRGs (Figure 2).

Histological Assessment of the Brain of *Ndrg1*-deficient Mice

We previously reported the phenotypes of *Ndrg1*-deficient mice (Okuda et al. 2004). They exhibited muscle weakness caused by peripheral nerve degeneration, but their complicated motor abilities were relatively retained. These phenotypes suggest that CNS can withstand the loss of NDRG1. According to the analysis of conventional histological sections,
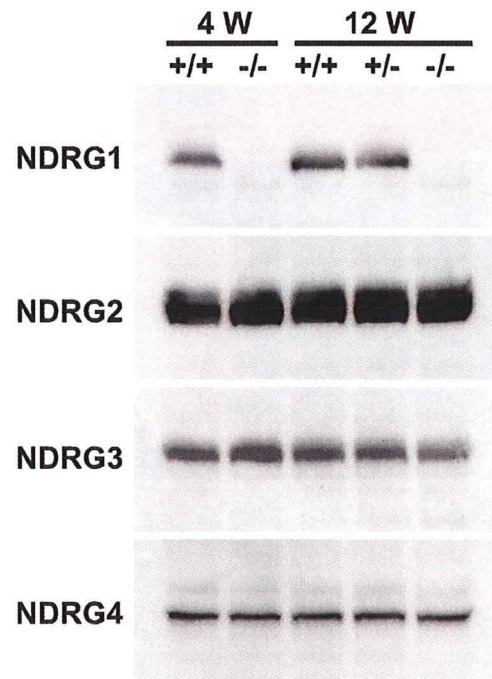

Figure 2 Expression of NDRG family proteins in the mouse brain. Brain lysates were prepared from the wild-type and *Ndrg1*-deficient mice aged 4 or 12 weeks and analyzed by Western blotting. Each lane contained 5 μg of total protein. [+/+], wild-type mice; [−/−], homozygous *Ndrg1*-deficient mice; [+/−], heterozygous *Ndrg1*-deficient mice.

no abnormalities were observed in the brain of *Ndrg1*-deficient mice (Figure 3). Organization of the cerebral cortices and other laminated regions seemed normal (Figures 3A and 3B). The structure of the hippocampus in the *Ndrg1*-deficient mice was not different from the wild-type one (Figures 3C and 3D). Luxol–fast blue staining for the myelin sheaths revealed that myelination was not affected in the brain of *Ndrg1*-deficient mice (Figures 3E and 3F). Immunohistochemical analysis of the wild-type mouse brain using anti-NDRG1 antibody exhibited specific staining in the axon bundles of the corpus callosum, corpus striatum, and fimbria hippocampus (Figure 3G). These NDRG1-staining signals were not detected in the *Ndrg1*-deficient mouse brain (Figure 3H).
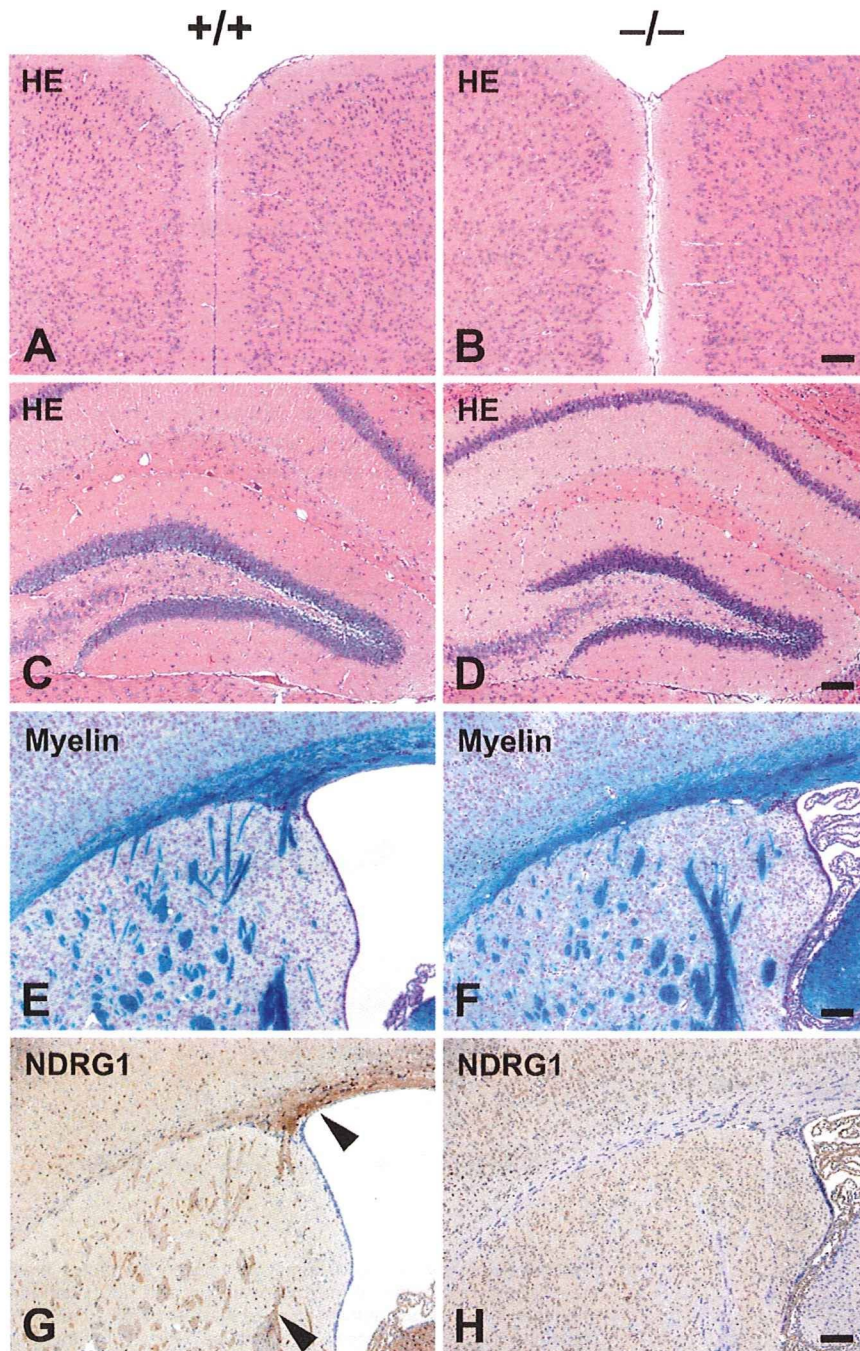
Figure 3 Histological assessment of the brain of adult *Ndrg1*-deficient mice. Transverse sections of cerebral neocortex (**A,B**) and hippocampus (**C,D**) of adult wild-type ($^{+/+}$; **A,C**) and adult *Ndrg1*-deficient ($^{-/-}$; **B,D**) mice were compared. There were no significant differences in the structure of the brain regardless of genotype. Transverse sections of the forebrain at the level of the corpus callosum (**E,F**) and lateral ventricle (**G,H**) of adult wild-type (**E,G**) and adult *Ndrg1*-deficient (**F,H**) mice were compared. Normal myelination was observed in wild-type (**E**) and *Ndrg1*-deficient mice (**F**). NDRG1 was detected in the axon bundles of the corpus callosum and corpus striatum in wild-type mice (arrowheads in **G**). NDRG1 expression was not detected in the *Ndrg1*-deficient mice (**H**). HE, hematoxylin–eosin staining; myelin, luxol–fast blue staining; NDRG1, anti-NDRG1 immunostaining. Bar = 100 μm.

Expression Patterns of NDRGs in the Brain

To investigate the expression characteristics of NDRGs in the brain, we performed immunohistochemical analysis using the antibodies specific for each NDRG. First, NDRG1 was strongly detected in the cytoplasm of oligodendrocytes in the cerebrum (Figure 4A). Specific expression of NDRG1 in the oligodendrocytes was confirmed by double staining for NDRG1 and CNPase. CNPase is a marker for oligodendrocytes (Figures 4C–4E). Although the cytoplasm was a principal site of NDRG1 localization, a fibrous staining pattern was also detected, suggesting that NDRG1 was partially localized in the processes of oligodendrocytes. In addition to the oligodendrocyte localization, weaker staining of NDRG1 was detected in Purkinje cells of the cerebellum (Figure 4B). NDRG1 was also strongly expressed in ependymal cells in the cerebrum (data not shown).

NDRG2 was strongly detected in the astrocytes of the cerebrum (Figure 5A), which was confirmed by double staining for NDRG2 and GFAP (Figures 5C–5E). GFAP is a commonly used marker for astrocytes. In the cerebellum, NDRG2 was also detected in Bergmann glial cells (Figure 5B). In both the cerebrum and cerebellum, NDRG2 was moderately expressed in most cells except neurons in the cerebral cortex and in Purkinje cells in the cerebellum (Figures 5A and 5B). Double staining for NDRG2 and NeuN indicated that NeuN-positive cells were NDRG2 negative in the cerebrum (Figures 5F–5H). NeuN is a marker for neurons. NDRG2 was less expressed in oligodendrocytes (data not shown). In the presence of immunogen peptides, anti-NDRG2 antibody did not give any signals (data not shown).

In contrast to the cytoplasmic localization of NDRG1 and NDRG2, expression of NDRG3 was observed in the nuclei of most cells in the cerebrum (Figure 6A). Nuclear localization of NDRG3 was also observed in other tissues (data not shown). Expression of NDRG3 was relatively strong in the neurons because most of the strong NDRG3-positive cells were NeuN-positive neurons (Figures 6C–6E). Significant expression of NDRG3 was also seen in the nuclei of Purkinje cells in the cerebellum, with less expression in the granule cells (Figure 6B). In the presence of immunogen peptides, anti-NDRG3 antibody did not give any signals (data not shown).

Expression of NDRG4 was detected in most brain cells, especially in the neurons of the cerebrum (Figure 7A, arrowhead) and Purkinje cells of the cerebellum (Figure 7B, open arrowhead). NDRG4-positive cells corresponded to cells expressing a neuron marker NeuN (Figures 7C–7E). NDRG4 was dominantly localized in the cytoplasm of these cells. Cytoplasmic localization of NDRG4 in Purkinje cells (Figure 7B) was similar to that of NDRG1 (Figure 4B). NDRG4 was less expressed in granule cells (Figure 7B) like NDRG1 (Figure 4B).

Discussion

Although NDRG1 is essential for structural and functional maintenance of myelin sheaths in the peripheral nervous system (PNS) (Okuda et al. 2004), the morphology of the brain was not affected by the loss of NDRG1 (Figure 3). To understand the tissue- and cell-specific roles of NDRGs, the localization of each NDRG should be clarified in detail. In the present study we developed specific antibodies and examined
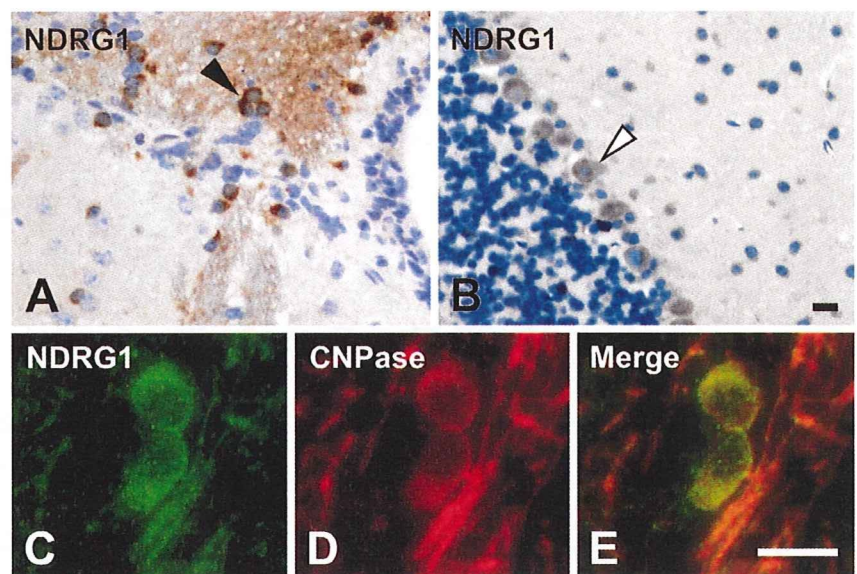
Figure 4 Localization of NDRG1 in the brain. NDRG1 was detected in the cytoplasm of the oligodendrocyte in the cerebrum (arrowhead in **A**) and in Purkinje cells in the cerebellum (open arrowhead in **B**). Expression of NDRG1 (**C**) was colocalized with an oligodendrocyte-specific marker CNPase (**D**). Merged image is shown in **E**. Bar = 10 μm.
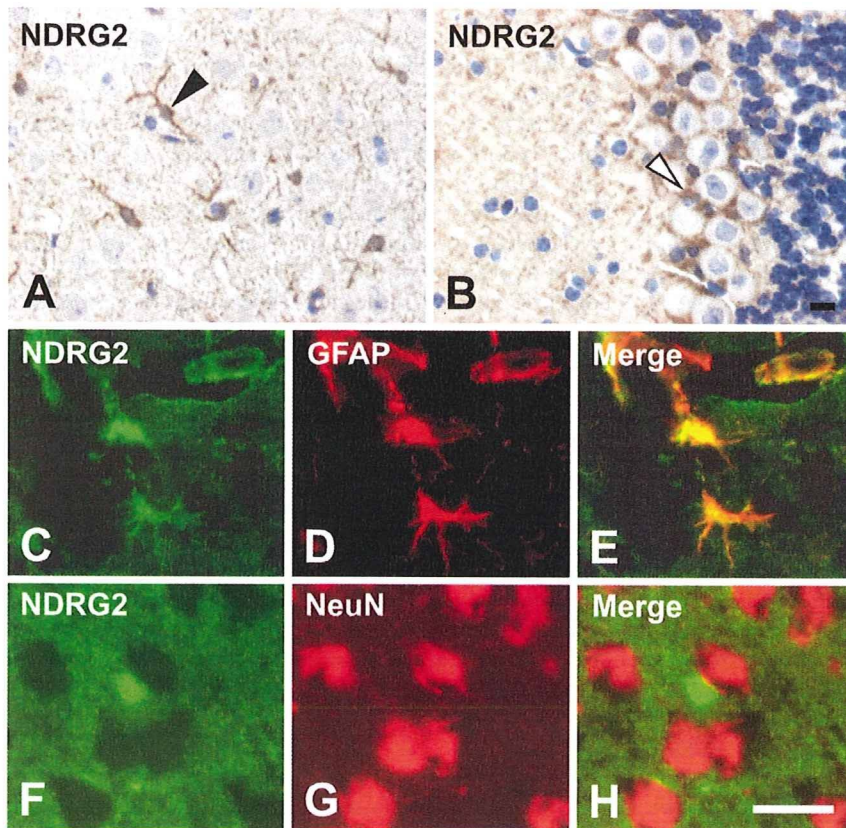
Figure 5 Localization of NDRG2 in the brain. NDRG2 was detected in the astrocytes in the cerebrum (arrowhead in **A**) and in Bergmann glial cells in the cerebellum (open arrowhead in **B**). Expression of NDRG2 (**C,F**) was colocalized with an astrocyte-specific marker GFAP (**D**), but not with a neuron marker NeuN (**G**). Merged images are shown in **E** and **H**, respectively. Bar = 10 μm.

the expression patterns of NDRGs in the mouse CNS. The expression patterns of each NDRG are summarized in Table 1.

Antibody specificity was examined by Western blotting analysis using recombinant NDRG–GFP fusion proteins. Each antibody specifically reacted with the corresponding protein, although the anti-NDRG1 antibody exhibited a weak cross-reaction to NDRG3 (Figure 1). This may be caused by a relatively high identity of NDRG3 to NDRG1 in amino acid sequence compared
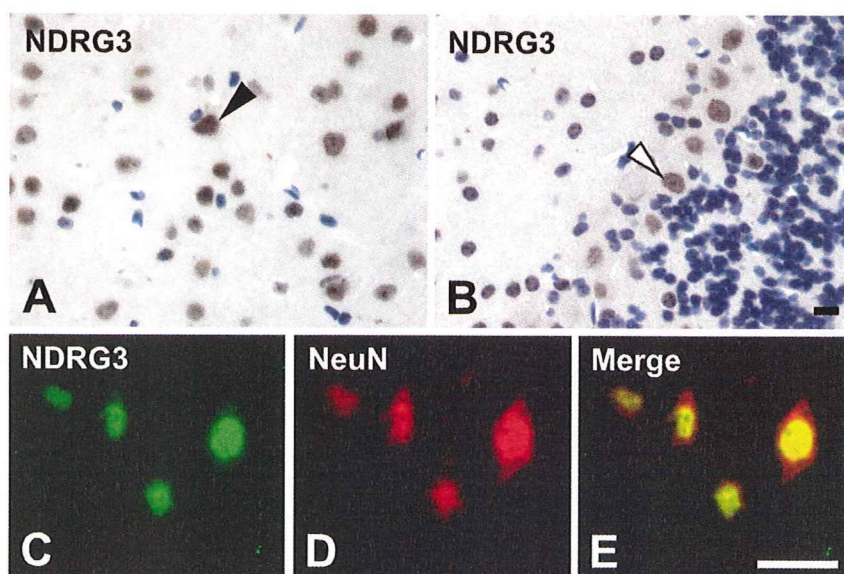

Figure 6 Localization of NDRG3 in the brain. NDRG3 was detected in the nucleus of most cells in the cerebrum, but especially strongly in the neurons (arrowhead in **A**) and nucleus of Purkinje cells in the cerebellum (open arrowhead in **B**). Expression of NDRG3 (**C**) was colocalized with a neuron marker NeuN (**D**). Merged images are shown in **E**. Bar = 10 μm.